Università Cattolica del Sacro Cuore
Sede di Brescia

Facoltà di Scienze Matematiche, Fisiche e Naturali
Corso di Laurea in Fisica

TESI DI LAUREA MAGISTRALE

Time and frequency resolved optical spectroscopy on Hg based high-Tc superconductors

Relatore:
Dott. Claudio Giannetti
Correlatore:
Dott. Gabriele Ferrini
Dott. Francesco Banfi

Laureanda: **Selene Mor**
mat. 3910178

Anno Accademico 2011/2012

You’ve got to dig to dig it, you dig?

Thelonious Monk

Contents

Chapter 1

Introduction

The discovery of copper-oxides superconductors at the end of 80s opend the era of *high-*T_c*superconductors*, changing the

Chapter 2

Conventional and unconventional superconductivity

In conventional metals the scattering between electrons and lattice vibrations is the microscopic mechanism that explains the transport and the optical properties. At low temperatures the electron-phonon coupling is responsible for the formation of the so-called *Cooper electron pairs* leading to the instability of the normal gound state. Therefore the system reaches a new state of equilibrium by performing a phase transition to the superconducting condensate. While the phonon-mediated interaction provides a full explanation of the behavior of conventional supercontuctors, whose transition temperature if of the order of a few degrees, this model fails in case of high temperature superconductors (HTSC), whose critical temperature is of the order of tens of degrees. What happens microscopically in this materials still remains unclear, but a common feature of these compounds is that they are affected by strong electronic correlations. Optical spectroscopy is an efficient technique in order to investigate the role of this interactions regardless of other contributions thanks to its wide spectral and ultrafast time resolution. In this chapter we present the Bardeen-Coopper-Schrieffer theory of superconductivity that accouns for conventional superconductors, with a focus on the phonon-mediated

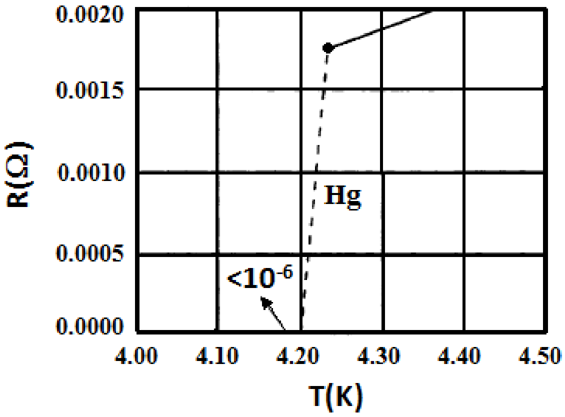

Figure 2.1: First experimental evidence of the superconducting transition [6].

electron-electron interaction. Then we discuss the main features of high critical temperature superconductors, with emphasis on differences with respect to conventional superconductors. Thus we describe statical optical properties of matters and their relation with the dielectric function by dealing with two models: the classical Drude-Lorentz model for metals and the extended Drude model for HTSCs.

2.1 BCS theory of superconductivity

Superconductivity was discovered in 1911 by H. Kamerlingh Onnes in Leiden laboratories. He observed that the electrical resistance of various metals dropped to zero in a small temperature range at a critical temperature T_c, which is characteristic of the material (see fig. 2.1). The second striking feature of superconductors was the perfect diamagnetism, found in 1933 by Meissner and Ochsenfeld: perfect diamagnetism means that not only a magnetic field is excluded from entering a superconductor, but also that a magnetic field, already penetrated the sample at $T > T_c$, is expelled outside as the sample is cooled through its critical temeprature (see fig. 2.2). More precisely, this Meissner effect implies that superconductivity can be destroyed by a magnetic field

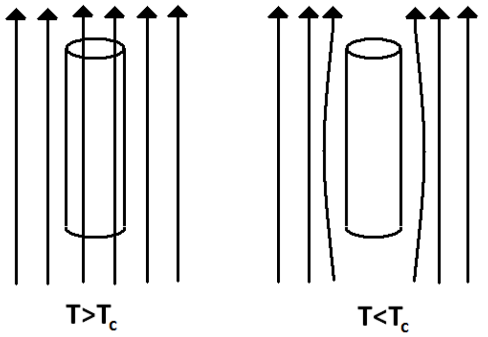

Figure 2.2: Expulsion of a weak external magnetic field from the interior of a superconductor ([1], page 668).

higher than a critical field H_c, which is related thermodynamically to the free-energy difference between the normal and superconducting phaes in zero field. This is called condensation energy of the superconducting phase. We point out that while the transition in zero field at T_c is of second order, the transition in the presence of a field is of first order since there is a discontinuous change in the thermodynamic state of the system and an associated latent heat.

For decades, the understanding of this phenomenon remained an unsolved puzzle, except for some fenomenological theories, the most meaningful of which are the London (1935) and the Ginzburg-Landau (1950) theories. Then, at the end of 1950s, a satisfactory theoretical picture of the classic superconductors emerged, merit of Bardeen, Coopper and Schrieffer. This situation was overturned in 1986, when a new class of high-temperature superconductors was discovered by Bednorz and Muller. These new superconductors seem to obey the same general phenomenology as the classic superconductors, but the basic microscopic mechanism still remains an open and contentious question.

In the Bardeen-Coopper-Schrieffer (BCS) theory, it was shown that below the critical temperature even a weak attractive interaction between electrons, such as that caused by the electron-phonon interaction at $\hbar\omega < \hbar\omega_{Debye}$, being $\hbar\omega = \hbar(E - E_F)$ where E_F is the ordinary Fermi ground state, causes an instability of the ordinary Fermi-sea ground

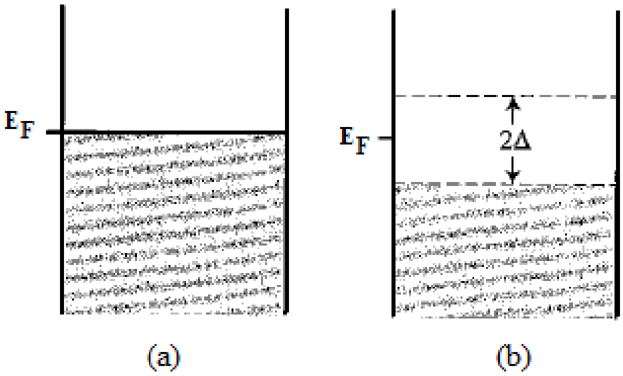

Figure 2.3: (a) Filled states in the normal state. (b) Formation of an energy gap, $E_g = 2\Delta$, in the superconducting phase ([3], page 212).

state of the electron gas with respect to the formation of highly-correlated pairs of electrons (*Cooper pairs*) occupying states with equal and opposite momenta and spins in an energy shell around the Fermi surface (see fig. (2.3)). One of the successful predictions was that the electron energy levels involved in the formation of such pairs form an incremental shell from radius $E_F - \Delta$ to $E_F + \Delta$, where $E_g = 2\Delta$ is the energy for the formation of a pair and corresponds to the energy gap, of order $K_B T_c$, that was already measured in many different experimental contexts. To give some examples, it was observed an effect of acoustic attenuation, according to which no damping of an impinging beam of phonons is observed if $\hbar\omega_q < 2\Delta$ at temperatures below T_c. Similarly, photons possessing energies less than 2Δ are not absorbed by the material in the superconducting phase, whereas they see a perfect resistanceless surface. By assuming a weak coupling description in accordance with the BCS theory, $\Delta \backsim 2K_B T_c$, and $\omega \backsim 4K_B T_c$. For a typical T_c of 5 K, $\omega \backsim$1 THz, i.e. in the infrared (IR). Thus IR radiation can penetrate the superconductor and scatter the electron, while a microwave beam is absorbed in order to provide the energy needed to create a pair. Experimentally, it was also observed that, if the ions were changed isotopically, the critical temperature changed accordingly in the same way as the frequencies of the phonon branches:

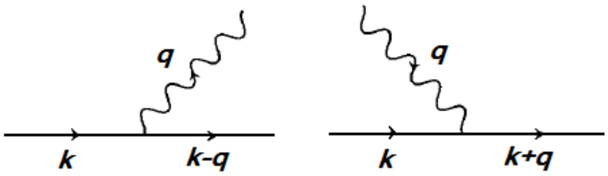

(a) (b)

Figure 2.4: Electron-phonon interactions: (a) through phonon emission; (b) through phonon absorbtion ([3], page 182.

$$T_c \propto \frac{1}{\sqrt{M}} \propto \omega_D. \tag{2.1}$$

This observation suggested that electron-phonon coupling should be really the microscopic mechanism at the origin of superconductivity.

2.1.1 Phonon-mediated electron-electron interaction

The origin of the pairing lies in an attraction between electrons, strong enough to overcome the Coulomb repulsion; this attraction is provided by the electron-lattice interaction or, quantum mechanically, by the electron-phonon coupling, which can occur in two ways, shown in fig. (2.4): by means of the emission or the absorption of a phonon. Since the condensation energy is of the order of a few meV while the Fermi energy for a metal is about 1-10 eV, we can treat the phonon mediated interaction between two electrons as a perturbation of an independent electron gas (*Fermi liquid*). What happens is that an electron interacts with the lattice and polarizes it; then a second electron interacts with the polarized lattice. This indirect interaction is described in fig. (2.5): in the first case, an electron with wave vector $\mathbf{k}$ emits a phonon of wave vector $\mathbf{q}$ and scatters in the state $\mathbf{k} - \mathbf{q}$; then the phonon is immediately absorbed by an electron with wave vector $\mathbf{k}'$, which will scatter in the state $\mathbf{k}' + \mathbf{q}$. electron. In the second case, a phonon

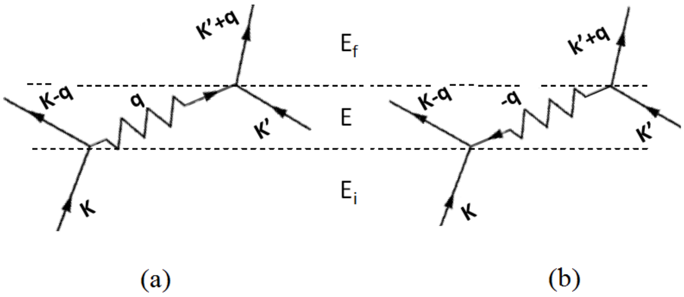

Figure 2.5: Rappresentations of the two electron-phonon interaction that provide electron coupling: (a) through phonon emission; (b) through phonon absorbtion [28].

with wave vector $-\mathbf{q}$ is emitted by an electron with wave vector $\mathbf{k}'$, that scatters in the state $\mathbf{k}+\mathbf{q}$. the phonon is immediately absorbed by a second electron with momentum $\mathbf{k}$, that scatters in the state $\mathbf{k}-\mathbf{q}$.

These two normal processes are equivalent and arise from the calculation of the second order perturbation of the electron-ion interaction potential:

$$V_{e\text{-}i}(q) = |M_q|^2 \left[\frac{\hbar\omega_q}{\left(E_k - E_{k-q}\right)^2 - \hbar^2{\omega_q}^2} + \frac{\hbar\omega_q}{\left(E_{k'-q} - E_{k'}\right)^2 - \hbar^2{\omega_q}^2} \right] \tag{2.2}$$

We observe that when the variation of the electron energy due to scattering is small compared to the energy of the phonon, the interaction potential $V_{e\text{-}i}$ is negative, i.e. it expresses an attractive character in the reciprocal space which results in the formation of bound electronic states, the Cooper pairs precisely. Thus the phonon mediated coupling mechanism is effective in an energy region of about $\hbar\omega_D$, where ω_D is the Debye cut-off phonon frequency. Since, as already said, that range of energies is severly limited compared to the values of the Fermi energy, the value of the potential $V_{e\text{-}i}$ is well approximated by a constant, negative value

$$V_{e\text{-}i} = \begin{cases} -V & |E_k - E_{k-q}| < \hbar\omega_D \\ 0 & |E_k - E_{k-q}| > t\hbar\omega_D \end{cases} \tag{2.3}$$

with $V > 0$.

Thus, in the picture of a Fermi electron gas subject to Pauli esclusion principle, the only levels involved in the interaction are those for which $E_F < E < E_F + \hbar\omega_D$. Suppose we are at T = 0 with the Fermi sphere completely filled and we add two electons with opposite momentum and spin orientation in one of that levels, thus they are affected by the attractive potential $-V$. The total energy of such system is thus lower than the total energy, $2E_F$, in case of absence of the potential. The energy gain related to the pair binding energy is equal to

$$E_g = \hbar\omega_D \frac{e^{-1/VN_0(E_F)}}{\sinh\left(1/VN_0\left(E_F\right)\right)}, \tag{2.4}$$

where we use a weak approximation for the density of states of the system, since $N_0\left(E_F\right)$ is actually the density of states for one spin direction, calculated for a unit cell in the normal state at the Fermi energy. In the weak-coupling limit, $VN_0\left(E_F\right) \ll 1$, we can rewrite the binding energy as follows:

$$E_g \simeq 2\hbar\omega_D e^{-2/VN_0(E_F)}. \tag{2.5}$$

Assuming that E_g is related to the energy of the superconducting transition, we had already observed that $E_g \approx K_B T_c$, then we have that T_c should be between 10^{-1} and 10^{-4} T_D (Debye temperature), depending on the intensity of the interaction, and this is compatible with the experimental observations.

It is interesting to observe that the larger is V, the larger is the energy associated with the formation of pairs, i.e. the larger is the scattering produced by phonons, the more advantageous is the transition to the superconducting phase. This implies that bad conductors in normal phase, i.e. materials with strong electron-phonon scattering, thus with high resistivity, have better superconducting properties, first of all a higher transition temperature T_c. This result is fully in agreement with the experimental observations, that are reported in fig. (2.6).

Before proceeding to the discussion of the high temperature superconductivity, we summerize the main features of BCS theory as follows:

- An attractive interaction between electrons can be lead to a ground state separated from excited states by an energy gap.
- The electron-lattice-electron interaction leads to an energy gap, $E_g \sim 2\Delta \sim 4K_BT_c$, of the same magnitude of the experimental one.
- The indirect interaction occurs when one electron interacts with the lattice and deforms it; then a second electron interacts with the deformed. In this way the second electron interacts with the first one via the lattice.
- The perfect conductance does not automatically imply perfect diamagnetism; it is the pairing mechanism, with the resulting gap in the excitation spectrum (and wavefunction modifications), that links in a unique destiny perfect conductance and perfect diamagnetism in superconducting materials.

2.2 High temperature Superconductivity

In 1986 the research on superconductivity was marked by the discovery of a new class of superconducting materials, namely high-Tc copper oxides (*cuprates*). First, Bednorz and Muller discovered that the $LaBaCuO$ compound became superconducting with a critical temperature $T_c \sim 30$ K. Then, intense research activity in copper oxides led to the synthesis of compounds with increasingly higher T_c. The most studied cuprates are

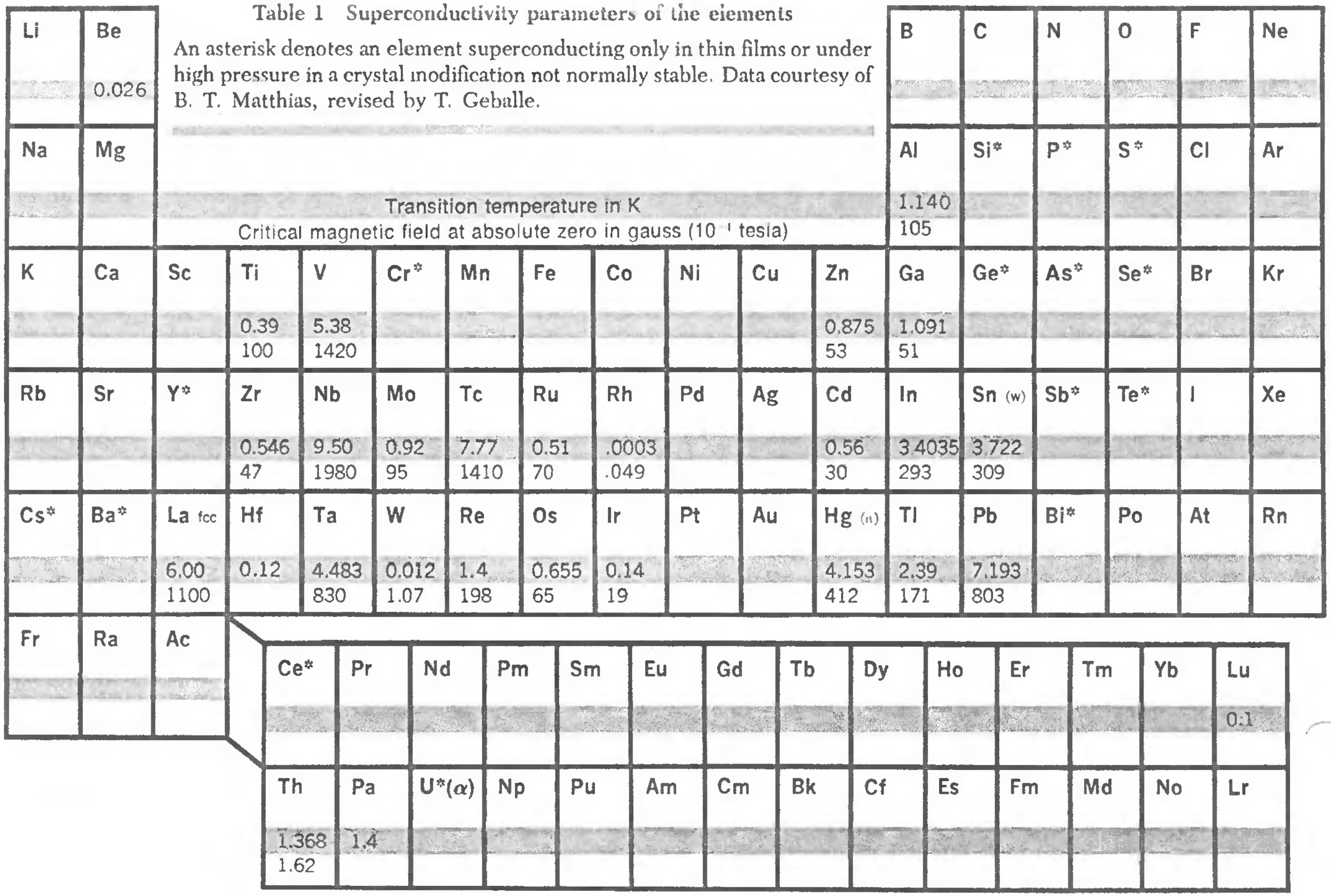

Table 1 Superconductivity parameters of the elements

An asterisk denotes an element superconducting only in thin films or under high pressure in a crystal modification not normally stable. Data courtesy of B. T. Matthias, revised by T. Geballe.

Transition temperature in K

Critical magnetic field at absolute zero in gauss (10^{-4} tesla)

Li	Be 0.026											B	C	N	O	F	Ne
Na	Mg											Al 1.140 105	Si*	P*	S*	Cl	Ar
K	Ca	Sc	Ti 0.39 100	V 5.38 1420	Cr*	Mn	Fe	Co	Ni	Cu	Zn 0.875 53	Ga 1.091 51	Ge*	As*	Se*	Br	Kr
Rb	Sr	Y*	Zr 0.546 47	Nb 9.50 1980	Mo 0.92 95	Tc 7.77 1410	Ru 0.51 70	Rh .0003 .049	Pd	Ag	Cd 0.56 30	In 3.4035 293	Sn (w) 3.722 309	Sb*	Te*	I	Xe
Cs*	Ba*	La fcc 6.00 1100	Hf 0.12	Ta 4.483 830	W 0.012 1.07	Re 1.4 198	Os 0.655 65	Ir 0.14 19	Pt	Au	Hg (α) 4.153 412	Tl 2.39 171	Pb 7.193 803	Bi*	Po	At	Rn
Fr	Ra	Ac															
			Ce*	Pr	Nd	Pm	Sm	Eu	Gd	Tb	Dy	Ho	Er	Tm	Yb	Lu 0.1	
			Th 1.368 1.62	Pa 1.4	U*(α)	Np	Pu	Am	Cm	Bk	Cf	Es	Fm	Md	No	Lr	

Figure 2.6: Table of elements with superconductivity parameters: critical temperature, critical field and resistivity in the normal state. We note that best conductors, such as Cu, Ag, Au, do not show superconductivity properties while worst materials have high resistivity in the normal state, but they become superconductors at higher temperature: a proof of the relevant interplay between electron-phonon scattering and superconductivity. [4]

$YBa_2Cu_3O_{6+x}$ (YBCO), which has maximum $T_c \sim 93$ K, and $Bi_2Sr_2Ca_1Cu_2O_{8+x}$ with maximum $T_c \sim 95$ K. At present, the highest observed value of T_c is about 150 K and is for the $HgBa_2Ca_2Cu_3O_{8+x}$ compound under pressure. These very high transition temperatures were of obvious technicological interest because they opened the way to applications which required only liquid N_2 cooling (77 K), rather than liquid helium.

Cuprates are strong correlated systems, i.e. the behavior of their electrons cannot be described effectively in terms of non-interacting entities, hence the single-particle approach of the quantum theory of solids (in the form of one-electron band theory) fails in providing a theoretical explanation of the high Tc superconductivity and the BCS model itself doesn't account for such materials, since it relies on the Fermi-liquid theory which cannot be applied to the cuprates in their normal state. On the other hand, in all of these systems, copper oxide planes form a common structural element, which is thought to dominate the superconducting properties: electrons partecipating in the superconducting condensate move indeed within weakly coupled copper-oxide layers.

The experimental evidences common for all the cuprates, and different from the BCS materials, are:

- an almost bidimensional crystal structure that causes strong anisotropy, whereas conventional superconductors show high simmetric structures (generally FCC or BCC). This anisotropy is strongly related to their high critical temperature through the 2D density of states;
- unconventional d-wave symmetry of the superconducting gap, revealed by Angle Resolved Photoemission Spectrocopy (ARPES) [14]. According to the definition of the gap parameter $\Delta_{\mathbf{k}}$ in terms of paired occupancy of all states **k'**:

$$\Delta_{\mathbf{k}} \propto < c_{\text{-}\mathbf{k}\downarrow} c_{\mathbf{k}\uparrow} > \propto -\sum_{\mathbf{k'}} V_{\mathbf{kk'}} < c_{\text{-}\mathbf{k'}\downarrow} c_{\mathbf{k'}\uparrow} >, \tag{2.6}$$

where $V_{\mathbf{kk'}}$ characterizes the strength of the potential for scattering a pair of electrons with opposite momenta (**k'**,**-k'**) to opposite momenta (**k**,**-k**). Assuming an isotropic system as in the BCS paring model, $\Delta_{\mathbf{k}}$ is independent of **k** and can be simply approximated as $-V$ over a range of energies near E_F: because of the spherical symmetry, this is often referred to as s-wave pairing. If the material is anisotropic (like YBCO), one expects that $\Delta_{\mathbf{k}}$ will no longer be isotropic, but that its dependence on **k** will have the same or maybe also a lower symmetry as the underlying crystal symmetry: actually, the degree of symmetry of the matrix elements $V_{\mathbf{kk'}}$ will be reflected in the symmetry of $\Delta_{\mathbf{k}}$ [2];

- occuring of a state called pseudogap [14], in which there is an anisotropic gap in the density of states, but the system does not exhibit any macroscopic superconductivity;
- an intrinsic inhomogeneity of the superconductiv phase on nanometric scale, as shown by STS measurements;
- at present there is still no real consensus as to the mechanism causing high-T_c superconductivity in these materials.

Regarding last point, we pinpoint two main streams choosen among all the suggested possibilities that can be found in the literature: a group of theoretical works relies on the idea that the electronic correlations are fundamental in the onset of the superconductivity [5], whereas a second hypotesis is based on a BCS like bosonic glue mechanism [24]. In this complex scenario, the question of d-wave pairing is central because microscopic mechanisms based on the exchange of antiferromagnetic spin fluctuations have been proposed, which would lead to $d_{x^2-y^2}$ pairing. The experimental proof of a d-wave pairing would support to such theories while it would exclude theories which were incompatible with d-wave pairing.

2.3 Equilibrium Optical Properties of high-Tc superconductors

Optical properties of solids, such as the reflectivity and the transimittivity, are experimentally accessible quantities and can be use to extract the optical constants of the materials, i.e. the complex conductivity $\sigma\left(\omega,T\right)$, or equivalently the complex dielectric function $\epsilon\left(\omega,T\right)$.

Since relfectivity and trasimmisivity are real quantities, while $\sigma\left(\omega,T\right)$ and $\epsilon\left(\omega,T\right)$ are complex, it is not trivial to understand how these quantities are related to each other. The complex dielectric function describes the interaction of electromagnetic radiation with matter as function of the frequency of the light and the temperature of the medium. When light of suffcient enegy shines onto a material, it induced transitions of electrons from occupied states below the Fermi energy to unoccupied states above the Fermy energy. Thus $\epsilon\left(\omega,T\right)$ depends strongly on the electronic band structure of the material.

The real part $\epsilon_1(\omega,T)$ accounts for the light propagation in the medium, while the immaginary part $\epsilon_2(\omega,T)$ is related to the absorption. They are not indipendent but rather they satisfy the Kramers-Kronig integral relations, that read

$$\epsilon_1(\omega) - 1 = \frac{2}{\pi} P \int_0^{\infty} \frac{\epsilon_2(\omega)}{\omega' - \omega} d\omega', \tag{2.7}$$

$$\epsilon_2(\omega) = -\frac{2}{\pi} P \int_0^{\infty} \frac{\epsilon_2(\omega) - 1}{\omega' - \omega} d\omega'. \tag{2.8}$$

These relations imply that any optical absorption is always accompained by light dispersion in the medium.

The complex refractive index $n(\omega)$ accounts for the processes of absorption and propagation through the real $n_1(\omega)$ and the immaginary $n_2(\omega)$ parts, respectively. The reflectivity $R(\omega, T)$ is in turn related to the complex refractive index. In particular, the normal incidence reflectivity is given by the following formula

$$R = \left| \frac{1-n}{1+n} \right|^2 = \frac{(1-n_1)^2 + n_2^2}{(1+n_1)^2 - n_2^2}. \tag{2.9}$$

As the refractive index and the dielectric function are related by

$$n^2(\omega) = \epsilon(\omega), \tag{2.10}$$

by means of Kramers-Kronig relations the reflectivity $R(\omega, T)$ can be espressed directly as a function of the dielectric constant $\epsilon(\omega, T)$ by the relation

$$R(\omega, T) = \left| \frac{1 - \sqrt{\epsilon(\omega, T)}}{1 + \sqrt{\epsilon(\omega, T)}} \right|^2. \tag{2.11}$$

Thus, by measuring experimental $R(\omega, T)$ over a wide spectral range, we are able to calculate both the refractive index and the complex dielectric fuction. Therefore, broadband optical spectroscopy provides a powerful tool to investigate the electronic properties of solids thanks to the frequency resolution of this technique.

In this chapter we need to introduce the equilibrium optical properties of cuprates. First we show the classical Drude-Lorentz model used to describe the conductivity in term of interband and intraband transitions of a classical gas of non-interacting electrons, then we consider the extended Drude model that accounts for strong electron-boson coupling in the intraband term of the equilibrium reflectivity of HTSCs.

2.3.1 The classical Drude-Lorentz model

In Fig. 2.7 we schematically show possible approaches toward an optical probe of interactions. The simplest model in the left panel treats the system as a classical gas of non-interacting particles and reduces the role of any interaction to a mild correction of optical properties in terms of a constant scattering rate τ and an effective mass m^* of fermions. This approach is adequately described by the Drude-Lorentz model and

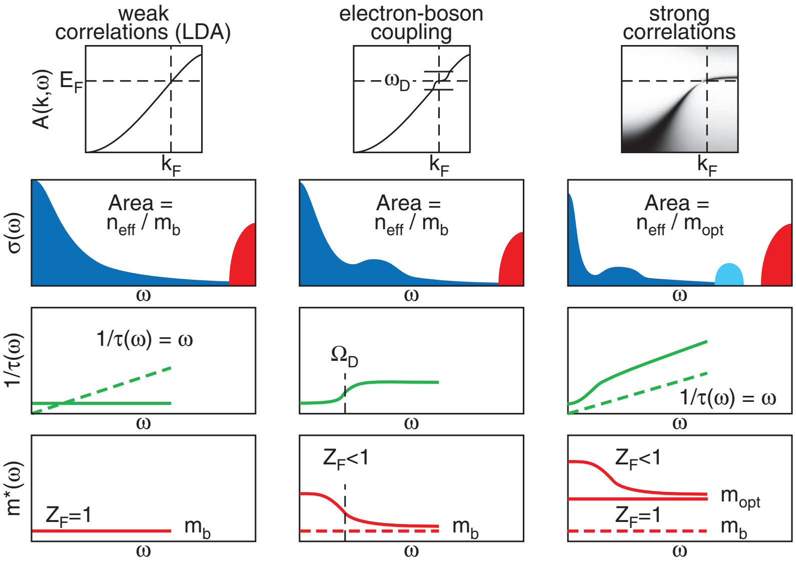

Figure 2.7: Schematic diagram revealing complimentary approaches to probing electronic correlations using optical methods. Top panels show the momentum-resolved spectral function in a non-interacting metal (left), weakly interacting system (middle), and strongly correlated system (right). Characteristic forms of the real part of the conductivity $\sigma_1(\omega)$, the frequency dependent scattering rate $1/\tau$, and effective mass m^* are displayed. [8]

is suitable for good conductors such as Alkali metals. Within this model, the optical conductivity $\sigma(\omega)$ is given by:

$$\sigma(\omega) = \frac{1}{4\pi} \frac{\omega_{p,D}^2}{1/\tau_D - i\omega\tau_D} + \frac{1}{4\pi \sum_i \frac{\omega_{p,i}}{\omega} i \left(\omega_i^2 - \omega^2\right) + \omega/\tau_i} \tag{2.12}$$

where the first therm (Drude term) is related to low-energy intraband optical transitions and describes the motion of the free carriers in the conduction band, $\omega_{p,D}^2$ being the Drude plasma frequency and $1/\tau_D$ the free carriers scattering rate. This term dominates in interaction of matter with infrared radiation and it is shown in the low energy broad peak in the second row of fig. 2.7. The second term accounts for high-energy interband optical transitions in terms of a sum of optical Lorentzian oscillators with characteristic plasma frequencies $\omega_{p,i}$, resonance frequencies ω_i and relaxation times τ_i. This contribution is also shown in fig. 2.7 by the red peak in $\sigma(\omega)$.

2.3.2 The Extended Drude Model

In case of strong interaction between electronic carriers and bosonic excitations, the Drude theory needs a generalization to the case of boson-assisted optical transitions. This model is called extended Drude model (EDM) and it is shown in the second column of fig. 2.7, in which Drude intraband contribution to the conductivity develops a "sideband" due to strong electron-boson coupling. The constant scattering time τ and the effective mass m^* are replaced by complex temperature- and frequency-dependent quantities.

Before going further with a more detailed explanation of EDM, let us hint the last case of strong correlated systems in which Coulomb repulsion dominates over all other processes. The right panels in Fig. 2.7 exemplify the characteristic electronic dispersion and typical forms of the optical functions for a correlated metal. We see that the oscillator strength of the entire intraband contribution is suppressed with the spectral weight transfer to the energy scale of the order of Coulomb energy and of interband transitions. What makes these correlation effects of great interest is that they are believed to be at the heart of many yet unsolved enigmas of contemporary physics including high-Tc superconductivity.

Let's go back to EDM: all the effects of strong interactions are accounted by the memory function $M(\omega, T)$

$$M(\omega, T) = M'(\omega, T) + iM''(\omega, T) = \omega\lambda(\omega, T) + i\frac{1}{\tau(\omega, T)}. \tag{2.13}$$

The immaginary real part of the memory function is simply related to electron-phonon scattering, while the real part accounts for the renormalization of the electronic effective mass due to strong correlations: the parameter λ quantifies indeed the strength of the interaction, leading to an enhancement of the effective mass compared to the Drude band mass as

$$m^*(\omega, T) = m_b[1 + \lambda(\omega, T)]. \tag{2.14}$$

The $M(\omega, T)$ is taken into account by the complex conductivity $\sigma(\omega, T)$ that reads

$$\sigma_D(\omega, T) = \frac{i}{4\pi}\frac{\omega_p^2}{M(\omega, T) + \omega} = \frac{1}{4\pi}\frac{\omega_p^2}{\frac{1}{4\tau(\omega,T)} - i\omega(1 + \lambda(\omega, T))} \tag{2.15}$$

while the complex dielectric function $\epsilon_D(\omega, T) = (4\pi/i\omega)\sigma_D(\omega, T)$ is given by

$$\epsilon_D(\omega, T) = 1 - \frac{\omega_p^2}{\omega(M(\omega, T) + \omega)} = 1 - \frac{\omega_p^2}{\omega(\omega(1 + \lambda(\omega, T)) + i/\tau(\omega, T))}. \tag{2.16}$$

The real and immaginary parts of these two sets of optical constants are related by analytic expressions

$$\sigma_1(\omega) = \frac{\omega}{4\pi}\epsilon_2(\omega) \tag{2.17}$$

and

$$\sigma_2(\omega) = -\frac{\omega}{4\pi}\left[\epsilon_1(\omega) - 1\right]. \tag{2.18}$$

The renormalized scattering rate and effective mass can be directly extracted from the optical conductivity, through the relations

$$1/\tau(\omega, T) = \frac{\omega_P^2}{4\pi} Re\left(\frac{1}{\sigma_D(\omega, T)}\right) \tag{2.19}$$

and

$$1 + \lambda(\omega, T) = -\frac{\omega_P^2}{4\pi} Im\left(\frac{1}{\sigma_D(\omega, T)}\right). \tag{2.20}$$

A good approximation of the memory function allows one to describe microscopically the coupling of electrons with phonons or other bosonic fluctuations by the convolution integral between the glue function $\alpha^2 F(\omega)$ and the kernel function $L(\omega, \omega', T)$:

$$M(\omega) = -2\int_0^\infty \alpha^2 F(\omega')\, L(\omega, \omega', T)\, d\omega'. \tag{2.21}$$

Strictly speaking, $F(\omega)$ is the phonon density of states, $\alpha^2(\omega)$ is a measure of the frequency-dependent electron-phonon interaction and $L(\omega, \omega', T)$ is a material independent function given by the Fermi-Dirac and Bose-Einstein distributions and describes the thermal depencence of the phononic excitations coupled with electrons. In order to evaluate other bosonic excitations the glue function must be adequately choosen.

Strong electron-boson coupling formalism is supposed to properly describe the optical response of an HTSC. Thus in cuprates the same formalism can be used, provided to replace the glue function with

$$\Pi\left(\omega\right)=\alpha^{2}\left(\omega\right)+I^{2}\chi\left(\omega\right), \tag{2.22}$$

which takes into account coupling both with phonons and spin-fluctuations. Once the convolution integral is calculated, it is possible to reproduce the measured complex conductivity and the complex diectric function through the relations (2.17) and (2.18).

Chapter 3

Hg1201: a prototypical high-$\mathbf{T_c}$ superconductor

The physical and optical properties of mercury-based high temperature superconductors are explained in this chapter. First we show the electronic propetries that are actually common to many HTSC compounds, since they are mainly determined by the copper-oxides layers present in all cuprates. Then we discuss the temperature-doping phase diagramm of HTSCs with a focus on the doping dependent features of these systems. Special attention is given to the pseudogap state in the last sectin of this chapter, since at present its physical origin constitutes one of the most challenging puzzle in the physcs of condensed matter.

3.1 Physical properties of Hg-based high $\mathbf{T_c}$ superconductor

Copper-oxide based high-temperature superconductors are a peculiar class of ceramic compounds with a perovskite-like layered structure, where a proper doping can induce superconducting phase transition at temperatures higher than any other superconduc-

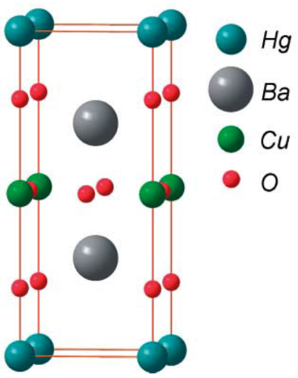

Figure 3.1: Schematic of the tetragonal Hg1201 crystal structure [26].

tor. This rich behavior is a consequence of the lamellar crystal structures, formed of copper–oxygen sheets separated by charge reservoir layers, and of the strong electron–electron correlations in the copper–oxygen sheets. In this thesis we worked on mercury-based cuprate compounds, namely the Hg1201 ($HgBa_2CuO_{4+\delta}$), with different degree of doping: an optimally doped sample with $T_c \sim 97$ K and an underdoped sample with $T_c \sim 55$ K.

3.1.1 Electronic structure

In Fig. 3.1 the crystal structure of a Hg1201 compound is shown. Hg1201 possesses a simple tetragonal crystal structure, with only one CuO_2 layer in the unit cell, and the highest maximum T_c of all known single-layer compounds. These properties, together with a wide accessible doping range and minimal effects of disorder, render Hg1201 an prototype for the study of the propetries of high-temperature superconducting systems. The electronic properties of cuprates are mostly determined by the Cu-O planes and are highly anisotropic when c-axis and ab planes are compared. Therefore, in the following, I will focus on the electronic structure of a single Cu-O plane, which is in common with all cuprates. The Cu^{2+} ions are in the electronic configuration $3d^9$ and the O^{2-} in the electronic configuration $2p^6$. The copper atom is surrounded by four oxygens

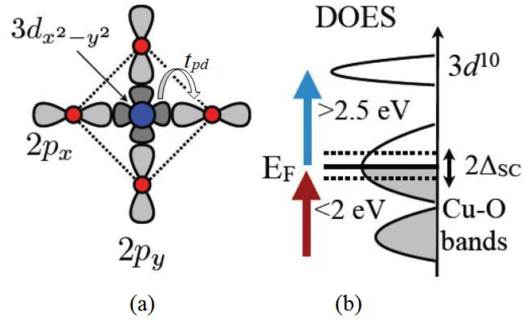

Figure 3.2: (a) Electronic orbilats responsible for the covalent bonding between Cu and O atoms in the Cu-O planes. (b) Density of states for Cu and O orbitals.

in the Cu-O plane and apical oxygens forming an octahedral lattice. The distortion from a perfect octahedron due to the shift of the apical oxygens splits the e_g orbitals so that the highest partially occupied d orbital is of the type x^2-y^2: this is known as Jahn-Teller effect. The lobes of this Cu orbital point directly to the 2p orbital of the neighboring oxygens, forming a strong covalent bond with a large overlapping between atomic orbitals. Thus the electronic state of the cuprates can be decribed by the so called *three band model*, where each unit cell has a singly occupied copper $d_{x^2-y^2}$ orbital and two doubly occupied oxygen p orbitals [16]. A simple sketch of the density of states is shown in Fig. 3.2.b.

According to band theory, a partially filled band would imply a metallic behavior of the system. In contrast, in the normal state, cuprates are antiferromagnetic insulators. The reason of the band theory's failure lies in the ignored strong electronic correlations (Coulombian repulsion) of these compounds. These are taken into account in the Mott-Hubbard model in terms of the strong repulsive energy cost U of having two electrons (or holes) on the same ion. Quantum-mechanically it is expressed by

$$U = \int |\phi_n(\mathbf{r}_1,t)|^2 \frac{e^2}{|\mathbf{r}_1 - \mathbf{r}_2|} |\phi_n(\mathbf{r}_2,t)|^2 d\mathbf{r}_1 d\mathbf{r}_2 \tag{3.1}$$

where $\phi_n(\mathbf{r}_1,t)$ and $\phi_n(\mathbf{r}_2,t)$ are the electron wavefunctions. Since electrons occupy delocalized states, such as s-states, the Coulomb repulsion is weak and can be ignored.

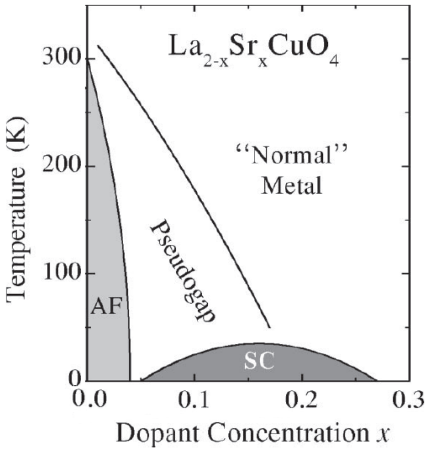

Figure 3.3: Phase diagram of hole doped superconductors [14].

As they occupy strong localized orbital, such as d-states, strong electron correlations occur. Thus the cost of filling the partially-occupied d-orbitals in the Cu-O planes of cuprates cannot be ignored. In the Hubbard model the overlap between atomic orbitals due to covalent bond is also taken into account and it is rapresented by the transfer integral t_{pd}, which accounts for the 'hopping' of electrons between neighboring sites (see Fig. 3.2.a). When electron repulsive energy U dominates over the hopping energy t, the ground state is an insulator because strong correlation effects prevent an electron from occuping the neighboring half-filled site.

3.1.2 Phase diagram

The physical properties of cuprates can be strongly modified by doping the samples, i.e. by injecting additional charges (electrons or holes) in these systems. There are mainly two ways of doping charge carriers into the Cu-O planes: by replacing different elements in the reservoir layers or by varying the oxygen content. If the copper oxidation state is varied by adding some oxygens between the Cu-O layers, a hole-doped superconductor is obtained.

The doping-dependent variation of physical properties is summerized in the phase diagram reported in fig. 3.3. The concentration of oxygen defects, x,varies from 0 to 30%. At zero added charges concentration the compound is an antiferromagnetic (AF) insulator at almost any temperature. Doping with oxygens results in a mean oxidation state of the copper atoms slightly grater than +2, i.e. the occupation of the d-orbitals decrease slightly by means of the virutal hopping of electrons between nearest-neighboring sites. Thus, at non zero doping the AF insulating state is suppressed since holes reduce the d-electrons localization due to strong Coulomb repulsion and the system shows a supercontucting behavior at temperatures lower than a critical value T_c that depends on doping concentration. The superconducting phase persists until about the 30% of hole doping concentration. The value of doping concentration corresponding to the maximal T_c represents the optimally doped condition. The region in the phase diagram with doping smaller than that corresponding to the maximum T_c is the underdoped region. In this region, heating above T_c, the system enters the so called pseudogap state. By further heating over a doping-dependent value T^* the system becomes a normal metal. Beyond optimal doping there is the overdoped region: here the pseudogap state disappears and the normal state shows a behavior closer to a Fermi-liquid.

3.1.3 The pseudogap state

Above T_c and in the underdoped region of the phase diagram an exotic state not found in the standard BCS superconductors appears. It is known as the pseudogap state. The pseudogap was first suggested by temperature dependence of the spin-lattice relaxation in nuclear magnetic resonance studies and it was interpreted as the opening of a pseudogap below a temperature $T^* > T_c$ [9]. A large number of experiments have been performed trying to understand the origin of the pseudogap state and the connection between the pseudogap and high T_c superconductivity or, in other words, between the two energy scales E_{PG} and E_{SC}. These and other questions concerning the pseudogap still remain unsolved.

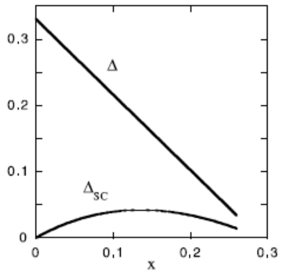

Figure 3.4: Trends of the two gap parameters as function of doping

Two are the main proposed scenarios. The first [17] assumes the existence of preformed Cooper pairs at temperatures just below T^*, that become phase coherent under T_c. The loss of coherence in the Cooper condensate is explained in term of phase fluctuations that, due to the low density superconducting carriers, may prevent a long range even if Cooper pairs persist above T_c. In this scenario the pseudogap would be considered only a phase anticipating the transition between the normal state and the superconducting phase. In the second scenario, the pseudogap is considered a new phase with different physical properties and a different ground state with respect to the normal state. Thus a new theory has to be develop in order to explain the onset of a superconducting state from this pseudogap ground state. As the BCS theory, so successfully developed for describing conventional superconductors, does not seem to have the appropriate foundation for the description of high-T_c superconductivity, so also the quantum theory of solids itself, in the form of one-electron band theory, has proven inadeguate for HTSCs, since the strong electron correlations prevent to deal with HTSCs as Fermi-liquid-like metals. Actually within this scenario two hypothesis come forwards: or the pseudogap has only different properties but any new order parameter has to be include in describing these properties, nor the pseudogap coincides with the appearance of a new order parameter, thus the pseudogap has to be identify as a really new phase of the system. Different order parameters have been proposed [10, 23], such as magnetic **??** or density-wave orders **??**.

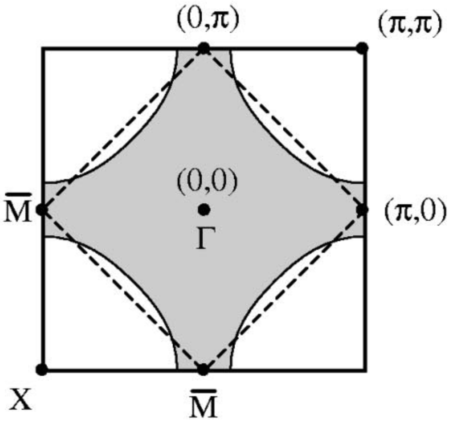

Figure 3.5: First Brillouin zone of $La_{2-x}Sr_2CuO_4$ high-T_c superconductor [14].

Insipite of different scenarios, from a wide variety of techniques, i.e. by measuring different physical quantities, a foundamental conclusion can be drawn: the HTSC phase diagram is dominated by two energy scales identified by T_c and T^*, which are well separated in strong underdoped compounds and converge to the same critical point at the end of the superconducting dome. Measurements performed on different compounds but with almost the same T_c show very similar temperature trends of the two energy scales as function of the doping. The schematic trend is shown in fig. 3.4. The coexistence of two scale is essential since the pseudogap reflects the pairing strength and the second the superconducting condensation energy.

One of the most direct low-energy probe is the angle-resolved photoemission (ARPES) [19]. Through this technique the pseudogap manifests itself as a suppression of the normal-state electronic density of state at the Fermi surface. This suppression is larger along the antinodal direction of the Brillouin zone, i.e. around (π,0) and vanishes along the nodal direction, i.e. the (0,0) to the (π,π) line (see the Fig. 3.5). We note that the antinodal direction corresponds to the square side of the direct lattice, while the nodal direction to the diagonal. Thus an anisotropic gap in the density of states appear along the direction where electron are closer, i.e. where they experience stronger correlations.

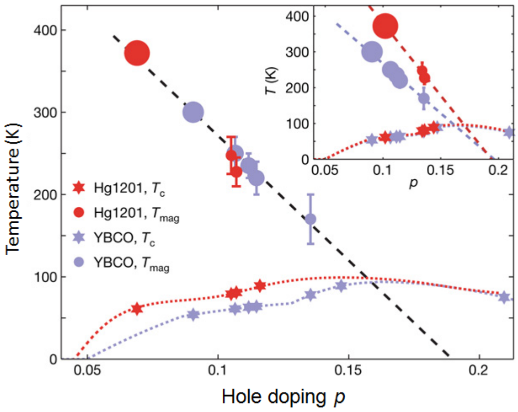

Figure 3.6: Universal pseudogap state diagram of Hg1201 and YBCO [20]

From the momentum dependence of the excitation gap along the Fermi contour, two distincs components emerge: the superconducting gap and the pseudogap. The first dominates the response in the nodal region, while the pseudogap at the anti-node.

Since ARPES and other equilibirum spectroscopies, such as STM and Raman scattering, provide a tool to investigate low-energy electronic excitation, optical spectroscopy is a complementary technique since it allows one to understand whether and how the high-energy scale physics is involved in the pseudogap phase formation. Therefore in this thesis broadband optical spectroscopy is used to investigate the electronic properties of the pseudogap phase in hole-doped mercury-based compounds, whose phase diagramm is shown in Fig. 3.6. The pseudogap of the optimally doped sample lies in a narrow interval of temperatures above T_c= 96 K: we will show in section 5.3.3 that we were able to drive the sample out of the pseudogap state by simply heating it at temperature about 170-180K. The second investigated sample is an underdoped compound with a lower critical temperature (T_c= 55 K) and a much larger interval of temperature in which it remains in the pseudogap state. By looking at the diagram, the end of the pseudogap would be at $T^* \sim 370$ K, which is higher than the temperature we were able to reach because of heater range limitation of out experimental set-up. However, our

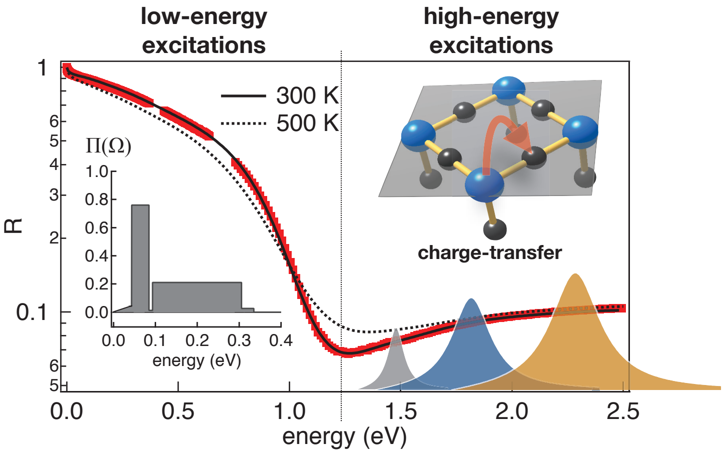

Figure 3.7: Reflectivity of the Y-Bi2212 crystal at optimal doping (Tc=96K), as measured by conventional spectroscopic ellipsometry (red dots). The reflectivity is well reproduced by an extended Drude model and a sum of Lorentz oscillators (black line). The total bosonic glue, $\Pi(\omega)$, extracted from the data is shown in the left inset. The dashed black line represents the reflectivity calculated for the same system at T=500 K. [15]

data confirm the presence of a pseudogap state in the system up to a temperature of $T=$ 350 K as expected.

3.2 Equilibrium reflectivity of Hg1201

In order to fit our reflectivity data at equilibrium, the glue function (2.22) must be known. A widely studied compound, which is very similar to the Hg1201, is the $Bi_2Sr_2Y_{0.08}Ca_{0.92}CuO_{8+\delta}$ (Y-Bi2212) crystal. This cuprate has indeed the same critical temperature T_c at optimal doping as that of the Hg1201. Thus, in orded to discuss the equilibirum reflectivity of cuprates we keep as reference the reflectivity data and the modeled glue function of Y-Bi2212. In Fig. 3.7 we see that the reflectivity of a Y-Bi2212

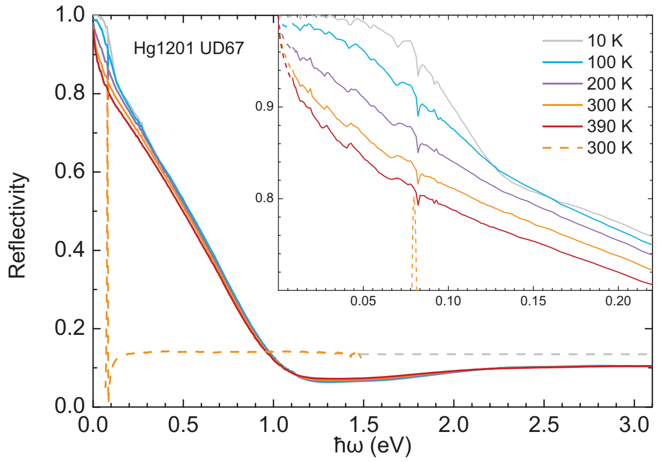

Figure 3.8: Equilibrium reflectivity of an underdoped HG1201 sample along the a (solid lines) and the c (dashed lines) axes is shown at different temperatures [21].

crystal, measured by spectroscopic ellipsometry at 300 K, is well reproduced by an extended Drude model with a broad peak below 1.25 eV, which is related to the optical response of the low-energy excitations in the conduction band, and a sum of Lorentz oscillators at higher energy, that account for the interband transitions. In the left inset the total bosonic glue extracted from the data is shown.

We note that the glue function exhibits a contribution at energy below 100 meV and a broad continuum that extends up to 300-400 meV. Since in cuprates the phonon energies have an upper limit at about 90 meV, the bosons involved in the interaction with the electrons cannot be only phonons. All contributions to the total bosonic glue function are taken into account by a sum of two terms: one due to phonon-mediated Cooper pairs, $\alpha^2 F\left(\omega\right)$, and one other that accounts for the coupling with all other bosonic excitation of electronic origin (i.e. spin fluctuations), $I^2\chi\left(\omega\right)$.

In Fig. 3.8 we report the infrared reflectivity R of the ab plane of an underdoped Hg1201 sample measured at near-normal incidence using a Fourier-transform spectrometer (8 meV - 1.24 eV). A temperature- independent phonon mode is observed at 82

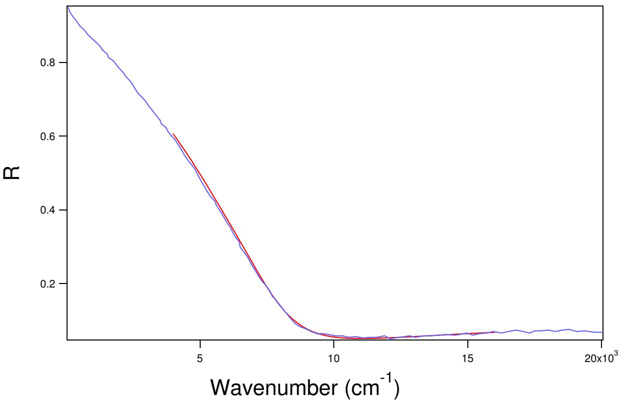

Figure 3.9: Equilibrium R data of an underdoped HG1201 and the best fit through EDM as functions of the photon wavenumber (cm^{-1}). The conversion in photon energy is 1 eV = 8064 cm^{-1}.

meV and the inset shows the far-IR reflectivity where also a *c*-axis phonon appears at 70 meV

We reproduce the equilibrium R data by the extended Drude model and a sum of four Lorentz oscillators: the best fit is shows in Fig. 3.9 and the corresponding parameters are summerized in the Tables 3.1.

The $\Gamma_{impurity}$ term accounts for the impurity scattering contribution due to some disorder in the system, such as lacks or fluctuation in the periodicity of the lattice.

As explained in chapter 2.3.2, the kernel function $L(\omega, \omega', T)$ is taken into account in the EDM through the memory function (see equation (2.13)). Since the kernel is a function of Fermi and Bose distributions, it depends on the temperature. The T_{eff} terms is refferred to an effective temperature of the system and at equilibrium is set at 40 K to reproduce the measurements performed in the superconducting phase, at 150 K for that performed in the pseudogap state and at 300K for measurements in the normal state.

The total bosonic glue function is determined by a block model, as that schown in the left inset of Fig. 3.7. The x_i identify the position of the blocks and P_i their heights. The $\epsilon_{infinity}$ term accounts for all contributions at "infinity" frequency, i.e. at very high energy; it should be equal to 1 in the case we considered a large number of Lorentzian oscillators. In order to reduce this number to only four oscillators, this value is chosen higher than 1. The four oscillators describes the high energy interband transitions and are characterized by three parameters: the position or resonance frequency, ω_i $(i = 1, 2, 3, 4)$, the spectral weight $\omega_{p,i}$ and the linewidth Γ_i. In case of high temperature cuprate superconductors, the Drude contribution is described by the EDM parameters shown in table 3.0(a), while interband transitions above 1 eV can be modeled with Lorentz terms, whose parametners are reported in table 3.0(b) .

3.3 Non-equilibrium properties of HTSCs

Since the electronic and phononic excitations coexist on the 0-90 meV energy scale, the determination of their relative weight to $\Pi(\omega)$ by means of equilibrium optical measurements remains elusive. Non-equilibrium optical spectroscopy provides a tool to overcome this limitation since it is able to prepare the system in a non equilibrium state, i.e. with the excited fermionic population decupled from the distribution of bosonic excitations, by means of ultrashort light pulse (pump). Then a second pulse is in charge of probing the temporal evolution of both distribution, as a function of the delay from the pump pulse. Thus adding the temporal resolution to the frequency resolved measurements, the dynamics of bosonic excitations of electronic and phononic nature can be disentangled on the basis of their different timescales while exchanging energy with the excited electrons.

(a)

Parameters	Values
$\epsilon_{infinity}$	2.52
ω_{plasma}	16576
$\Gamma_{impurity}$	20.062
T_{eff}	300
x_0	170
x_1	382
x_2	654
x_3	1411
x_4	2347
x_5	2900
P_0	9.6346e-06
P_1	1.12663
P_2	1.0196
P_3	0.056
P_4	0.22743
P_5	0.1464

(b)

Parameters	Values
ω_1	6183.1
$\omega_{p,1}$	1842.1
Γ_1	3441.2
ω_2	11866
$\omega_{p,2}$	2736.6
Γ_2	7000
ω_3	20184
$\omega_{p,3}$	12543
Γ_3	14499
ω_4	39468
$\omega_{p,4}$	32118
Γ_4	18121

Table 3.1: Fit Parameters: extended Drude model 3.0(a) and Lorentz oscillators 3.0(b).

Chapter 4

Experimental set-up & sample preparation

In this chapter we explain the main features of our experimental set-up and the techniques we used to prepare the samples and perform the measurements. First we provide a description of the pump and probe technique that allows us to investigate the non-equilibrium properties of matter thanks to high temporal resolution. Then we briefly discuss each component of the laser system and present the main parameters of the laser beam. In the third and fourth sections we show the infrared (IR) pump-supercontinuum probe and the one color pump-probe set-ups and their acquisition systems. Then we show the cooling and vacuum systems and we describe the sample preparation procedure.

4.1 Pump-probe technique

The goal of our work is to study the non equilibrium optical reflectivity of high-Tc superconductors, therefore we employ the so called *pump and probe technique*, which is currently the most efficient time-resolved optical spectroscopy. Traditional electronic

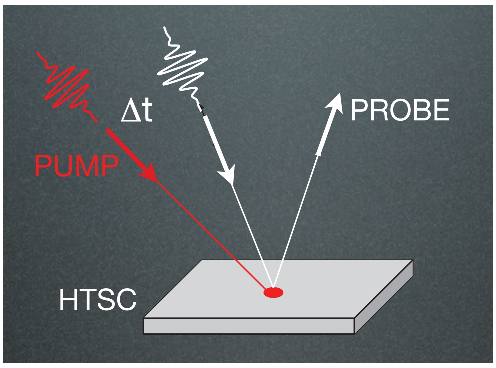

Figure 4.1: Schematic representation of the pump and probe experiment.

devices are not able to follow the dynamics of the evolution of the physical properties that vary on the timescale of a few picoseconds, because of their limitations in terms of temporal resolution. On the contrary, our laser pulses have femtosecond duration and this is the key feature thae enables to study the dynamics of the out of equilibrium optical response, such as reflectivity and transmission, with subpicosecond time resolution.

In a pump-probe experimental set-up, the Ti:sapphire output laser beam is splitted into two beams of different intensities: the most powerful is the pump and it is used to excite the system, while the weaker arrives at the same point of the sample, suitably delayed in time, and probes the variation of reflectivity induced by the pump. A schematic representation of a pump and probe experiment is shown in Fig. 4.1.

In order to compensate for laser intensity fluctuations, we measure the normalized variation of reflectivity

$$\Delta R(\tau) = \frac{R_{exc}(\tau) - R_{eq}}{R_{eq}}, \tag{4.1}$$

where τ is the delay between the two optical beams, $R_{exc}(\tau)$ is the reflectivity of the pump excited sample, R_{eq} is the reflectivity in the equilibrium state.

This technique is also characterized by the very high sensitivity in detecting of very small relative variations (on the order of 10^{-6} with respect to R_{eq}) thanks to lock-in acquisition system, that we will explain later in this chapter.

In addition, combining this experimental set-up with an optical fiber we are able to convert the infrared probe beam into supercontinuum light, achieving wavelenght resolution. Such measurements are of great interest in investigating condensed matter, because the optical response of the sample provides direct information about the dielectric function of the system, which depends on the electronic structure of the material.

Let us show in more details how this technique works. The two beams involved in the measurements cover different paths but these must be of the same lenght in order to fulfill the initial conditions of spatial and temporal coincidence on the sample. This means that, before starting the acquisition, we have to focus both pulses at the same point on the sample and to set the time delay between pump and probe in order to syncronize the arrival of both the pulses on the sample. For this purpose, a Micos Scan Delay device, consisting of a set of mirrors mounted on a motorized sledge, is located along the pump path. Taking into account the speed of propagation of light and the round trip of the scan devices , we obtain that an optical path difference equal to 1 μm corresponds to a time delay of 6.6 fs. The spatial coincidence, monitored by a CCD camera (Thorlabs), is required to probe the same area of the sample perturbed by the pump. This requirement force a condition on the spot sizes of the beams: to probe a uniformly excited zone of the superconductor, the spot size of the probe must be smaller than that of the pump and we obtain this by choosing different focal lenghts for each beam (longer for the pump beam, $f = 20$ cm, in order to be focused with a larger spot diameter than that of the probe, $f = 10$ cm).

4.2 Laser system

The scheme of our laser source is shown in Fig. 4.2. The first stage of the laser system is a solid-state diode-pumped Nd:Vanadate laser (Coherent Verdi V-10), which provides a

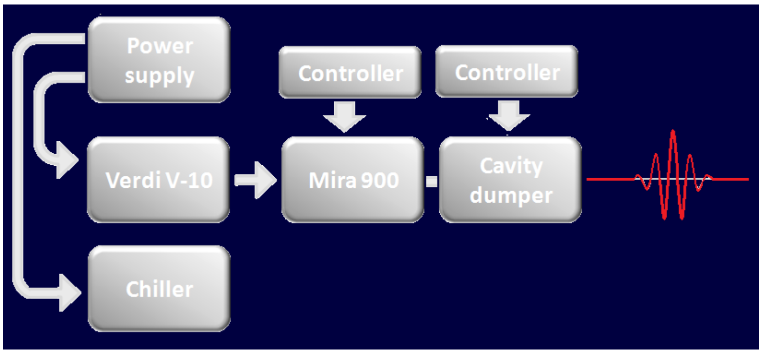

Figure 4.2: Laser System.

continuum monochromatic beam with wavelenghth λ= 532 nm and a maximum output power of 10 W, that acts as optical pump for the laser cavity (Coherent Mira 900). The Verdi V-10 laser consists of a laser head and a power supply connected to each other by an umbilical cable. A chiller is also connected to the Verdi V10, the temperature is set to 17°C. The Coherent Mira 900 laser is a Ti:sapphire oscillator, that converts the input continuous wave beam into a train of ultrafast pulses charaterized by a wavelenght λ= 800 nm with a narrow bandwidth of about 10 nm, a duration of 120 fs and a repetition rate of 76 MHz. The output beam has horizontal polarization (so p-polarization) and a TEM_{00} spatial mode. For a detailed explanation of the technique used to mode-lock the Mira laser, see appendix A.

To variably reduce the repetition rate and to even raise the output pulse energy, the cavity end mirror is removed and replaced by a totally reflecting mirror positioned inside a cavity dumper Pulse Switch. Its function is based on the optoacoustic effect, according to which a modulation of density, thus of refractive index, is introduced by an acoustic signal with high frequency, which is generated by appling an RF signal to a piezoelectric transducer cemented on the crystal. This acts as a syncronized optical grating on the laser beam coming from the Mira laser and passing the crystal, so the beam will be diffractes and single laser pulses can be periodically selected out of the pulse train, ready for usage in the experiment. The standard frequency of the Ti:sapphire combined

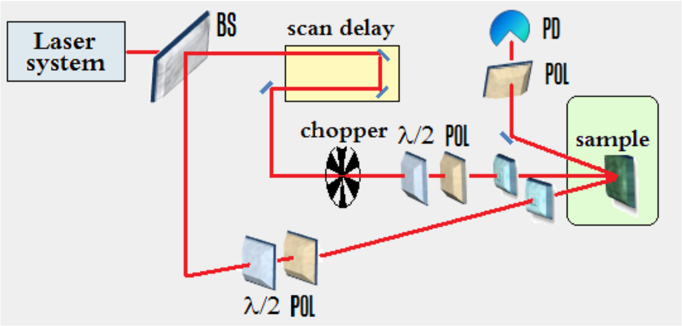

Figure 4.3: IR pump-probe experimental sel-up for lock-in acquisition. $\lambda_{pump} = \lambda_{probe} = 800nm$.

with the cavity dumper is 54.3 MHz, but the repetition rate is tunable as desired by setting the division rate (DR) from 30 (i.e. 1 pulse out every 30 ones, which corresponds to 1.81 MHz) to 26000 (i.e. 1 pulse out every 26000 ones, or 200 Hz).

The beam power reaches 250 mW in CW mode operation, while in ML modality it is of about 20 mW with DR=100, i.e. by setting the repetition rate to 54.3 KHz. With this configuration of parameters, the energy per pulse is about 40 nJ.

4.3 IR pump-probe set-up

This experimental set-up is shown in Fig. 4.3. First, an optical beam splitter is placed just out of the cavity in order to split the laser beam into two parts: 70% of the laser beam is transmitted and it is used as the pump pulse, while the 30% is reflected and acts as the probe. Thus both the pump and the probe are monochromatic, they have the same wavelenght of the output laser beam (λ=800nm) and, until now, they also have the same p-polarization. The intensity of both the lines is adjusted by means of a rotatable half-wave plate (λ/2 optical device), which introduces a phase shift between the polarization components of the electric field. Combining the λ/2 optical device with a polarizer, a rotation of beam polarization is obtained: the polarizer is oriented in order to obtain the desired polarization direction (vertical for the probe, horizontal for the pump), while the adjustment of the intensity is obtained by rotating the $\lambda/2$. The reflected probe beam is the signal and, in order to be detected, it is passed through a polarizer crossed with respect to the pump (in order to eliminate the scattering of the pump) and then it is focused on a silicon photodiode (Thorlabs DET210). The pump intensity is modulated in time (on/off) by a chopper rotating at a frequency of 3000 kHz.

The variation of reflectivity induced by the pump is extremly small and this constitutes a problem in the acquisition. In order to overcome this problem, we use a lock-in acquisition system, which is described in detail in appendix B. The frequency of the chopper rotation provides the frequency reference to the amplifier, that selects only the component of the reflected probe modulated at that frequency. The integration time for the lockin acquisition is conditioned by two constrains: it has to be longer than the chopper period, otherwise it can not acquire the entire intensity modulation, but not beyond the time of a scan, which is between 200 and 500 ms. In our measurements, the integration time is 5 ms. Thus we are able to acquire the small pump induced variation of the reflectivity, without the noise related to other frequencies.

At the end of this section we notice also that the signal of the photodiode is splitted into two: one enters the lockin amplifier, while the other is digitized and sent to the computer and it consitutes the continuum reflectivity signal, R_0.

4.3.1 Fluence dependent measurements - Pump power calibration

First we report some useful quantities related to laser beam.

- Pulse energy

$$E_P = \frac{P}{RepetitionRate} \tag{4.2}$$

where P is the average power of the laser beam, detected by a power meter.

- Fluence

$$F = \frac{E_P}{A} \tag{4.3}$$

  where A is the beam spot area, $A = \pi r^2$, where r is the radius of the spot. The fluence is a measure of the energy per surface unit released by each pulse on the sample.

- Pulse intensity

$$I_P = \frac{F}{\tau} = \frac{P}{A \cdot \tau \cdot RepetitionRate} \tag{4.4}$$

  where τ is the temporal duration of the pulse.

In order to get numerical values of all these quantities, we need first to know the beam spot diameter and the pulse duration: the first was estimated about 20 μm with knife-edge technique, while the second was measured of about 120 fs by means of autocorrelation.

In order to analyze the response of the system as a function of pump beam intensity, we need to calibrate the rotator of the half-wave plate located along the pump beamline. The set-up consisting in the half-wave plate and polarizer is in fact very sensitive to the rotation angle, particularly in corrispondence of the minimum values of transmitted pump power. Therefore we use a motorized rotator that allows one to obtain a sensitivity on angle setting of the order of 10^{-2} degree. The calibration is simply performed by acquiring pump beam while rotating about 45° the half-wave plate from the angle corresponding to maximum intensity by steps of half degree. Pump intensity as function of half-wave plate angle is fitted by a square cosin function and the calibration curves is shown in Fig. 4.4. By means of this plot we are able to choose the exact half-wave plate angle corresponding to the desired percentage of pump power we want to send to the sample.

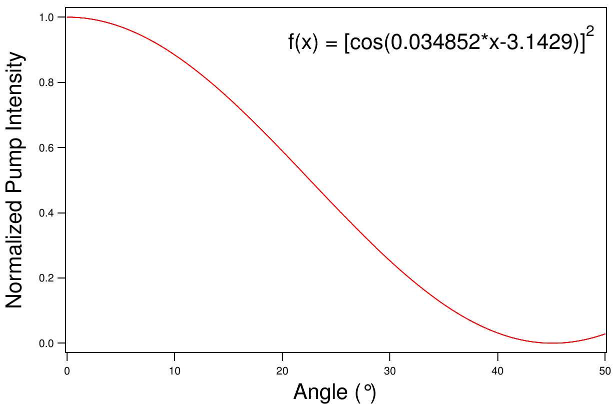

Figure 4.4: The normalized calibration curve of the rotator of the half-wave plate located along the pump beamline.

4.4 IR pump-Supercontinuum probe set-up

This experimental set-up is shown in Fig. 4.5. In this section we explain the main difference with respect to the previous case. In order to obtain photon energy resolution, the IR monochromatic probe beam is converted into supercontinuum light by passing through a non linar optical fiber (*Crystal Fibre FemtoWhite*) before going through the $\lambda/2$ optical device: the probe spectrum is broadened from 450 to 1600 nm. As shown in Fig. 4.6, an aspherical lens is used in order to focus the beam into the optical fiber and then an achromatic doublet is located just in front of the fiber to parallelize the output light, that has a divergence of about 20 degrees.

A prism is located along the optical line of the reflected signal: it is in charge of the dispersion of the reflected spectrum before it is acquired by a photodiode array, that replaces the silicon photodiode.

Because of the large difference between the scan frequency of the array and the repetition rate of the laser, it is necessary to integrate many pulses for the detection of the

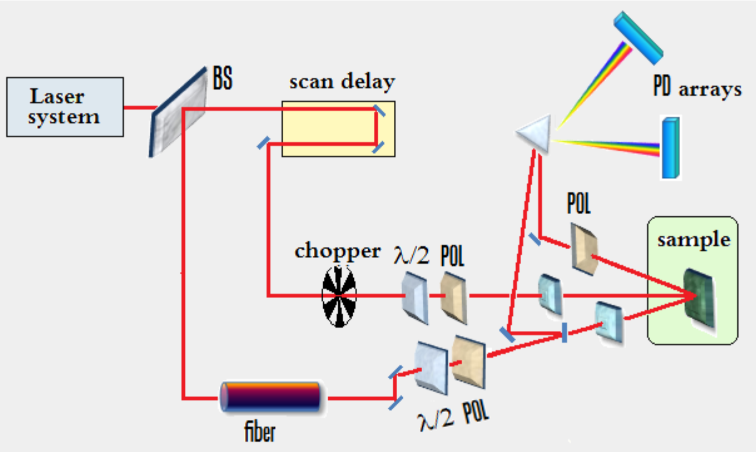

Figure 4.5: One color pump-supercontinuum probe experimental set-up.

Figure 4.6: Optical set-up for supercontinuum light generation: an aspherical lens in order to focus the monochromatic beam into the optical fiber for beam conversion into supercontinuum light and an achromatic doublet in order to parallelize the spectrum.

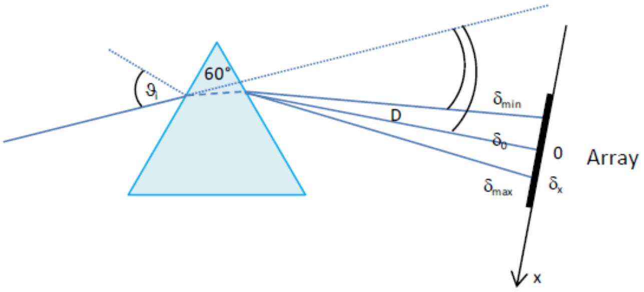

Figure 4.7: Dispersion of a supercontinuum beam through an equilateral triangular prism

transient reflectivity variation (low scanning method). Thus we need a reference signal, to compensate fluctuations of the intensity of the laser. We take the reference signal, through a beam splitter (8%r-92%t) located along the probe line just before the last focal lens: the transmitted part arrives on the sample, while the reflected part forms the reference. The latter passes through another prism and enters the reference array. Thus, both reference and reflectivity signals are simultaneously acquired by their respective arrays and the resulting measure is given by the ratio between them. Both the arrays are composed of 128 pixels (model Hamamatsu S8380-128Q). Each pixel of the arrays acquires a thin range of wavelenghts of the spectra that have been dispersed by the prism.

In order to reconstruct the frequency spectrum of the reflected signal, it is necessary to calibrate the arrays by assigning to each photodiode (to each pixel) the relative acquired wavelength, taking into account the non-linear dispersion of the polychromatic beam that passes through the prism (we use an equilateral triangular prism, see Fig. 4.7). The angular dispersion and the corresponding spatial deflection has been calculated so what we have to do for the calibration is first to filter the 800 nm wavelenght and to locate its dispersion in the middle of the array. Then we choose a pair of interferential filters: one for higher and one for lower wavelenght than 800 nm, according to the wavelenght range of our supercontinuum beam. The FWHM of the transmitted spectrum is of about 10 nm. We put the first filter along the probe line (between the optical fiber and the 8%-92% beam splitter) and we check the pixel at which the signal shows a maximum. Then we repeat the operation with the second optical filter. With this three landmarks, a Labview program is able to reconstruct the wavelenght calibration of both photodiode arrays: obviously, the wavelenght scale will not be linear. Notice that transmitted signals is much more dispersed for lower wavelenght, which in consistent with the dispersion curve, as shown in Fig. 4.8.

In this configuration it is not possible to use lock-in techniques for extracting the result of the pump-probe interaction from the total signal. In this case we measure the difference between the signal with and without excitation. This is achieved by modulating the pump beam with a mechanical chopper (rotation frequency is set at 25-30 Hz), and by acquiring the status of the modulation by means of a photodiode digitized by a data acquisition card (NI DAQmx M-series) which is synchronized with the digitizer. In this way it is possible to discriminate between pumped and unpumped pulses. At the end of a single acquisition the pump induced variational signal is obtained by mediating and subtracting the two signals.

4.5 Cryostat and vacuum system

To study the behavior of our samples in the superconducting phase we need to reach temperatures below their transition point. For this reason we use a cryostat coupled with a vacuum system (a Pfeiffer Vacuum turbomolecular drag pump) to achieve temperatures around 10 K at a pressure of 10^{-8} mbar. Our cryogenic refrigerator is closed-cycle and it is composed by an expander connected to a water-cooled helium compressor by two gas lines: one of the line supplies high pressure helium gas to the expander, the other gas line returns low pressure helium gas from the expander. The cryostat operates on the principle of the Gifford-McMahon cycle. It consists of 4 steps, as shown in Fig. 4.9:

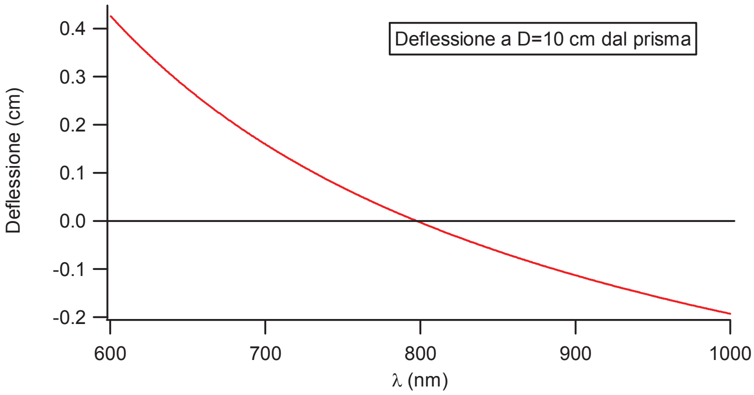

(a)

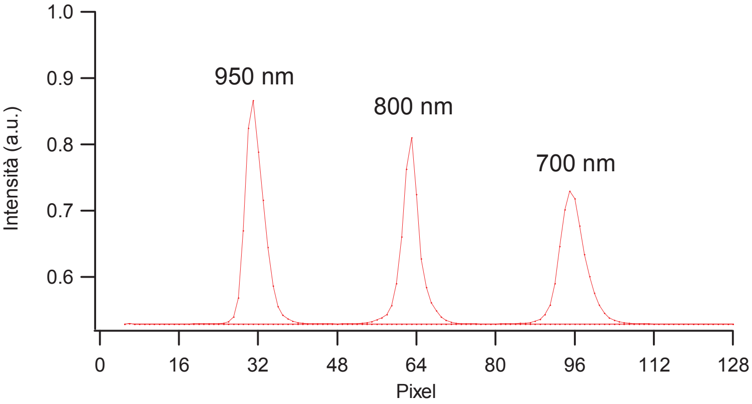

(b)

Figure 4.8: (a) Spatial deflection due to angular dirspersion of a supercontinuum beam passing through a prism. (b) Wavelenght calibration of a photodiode array. [28]

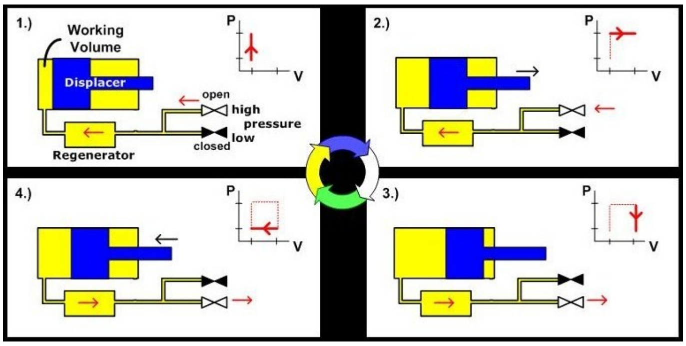

Figure 4.9: Gifford-McMahon Refrigeration Cycle. [29]

1. the low pressure valve is closed and the high pressure valve opened with fixed position of the displacer. The high pressure helium gas passes through the regenerator into the expansion cylinder: the pressure increases while heat is released;

2. the displacer can move, the gas expands at fixed pressure and cools;

3. the high pressure valve is closed and the low pressure valve opened with fixed position of the displacer. The gas flows through the regenerator toward the high pressure valve removing heat from the system.

4. the displacer moves to its original position forcing the gas to flow through the regeneretor. The absorbed heat is taken out through the low pressure valve.

At the end of this step we are back in position 1 and another cycle begins. Cycles are repeated until the chamber reaches the desired temperature that is setted and monitored by a temperature controller (Lake Shore 331 Model).

4.6 Sample preparation

Working on fresh and flat surfaces is crucial for optical measurements. These samples are tricky to deal with, both because they are too strong for simply scotch-tape cleaving and their surface degradets quickly by oxidation. Thus the surface preparation must be

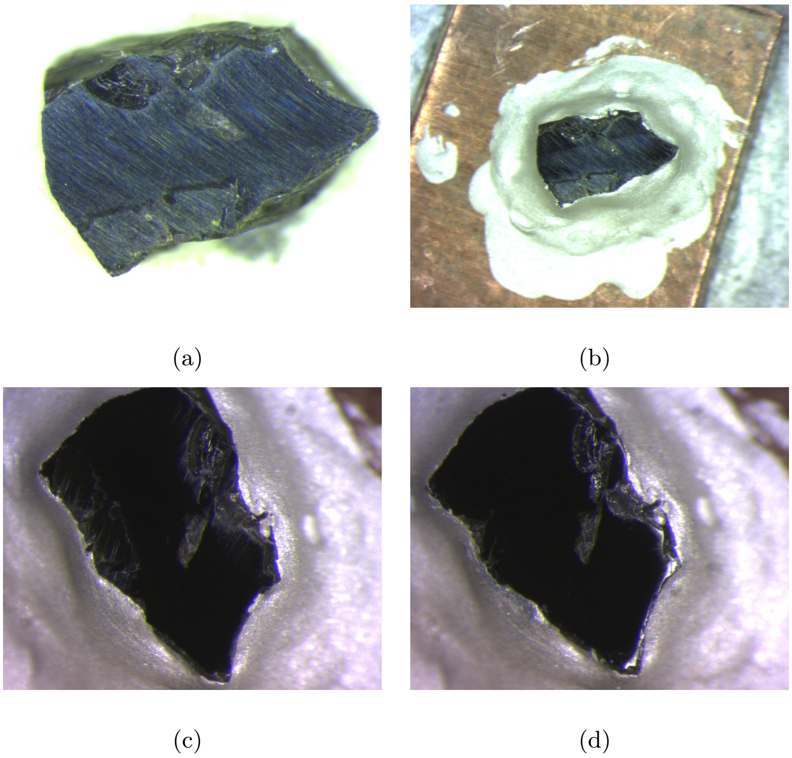
(a) (b) (c) (d)

Figure 4.10: Sample preparation step by step.

done with the crystals already glued with silver paste on a little coopper slab right before the measurements. What we did to obtain good surface in our samples was to keep part of the surface that was already cleaved (parallel to ab-plane) as the reference and polish the surface carefully under a microscope until all the surface is flat and parallel with that cleaved part (see Fig. 4.10). In order to confirm the right angle of polishing, the polished surface and the “cleaved” part (deeper and hence protected from polishing) piece were continuously being compared optically. For that we compared the reflection of the two surfaces with respect to a fixed spot light source under the microscope. We used 3M 263X polishing films with 0.3 micron grain, scotch-taped to a piece of thick glass to make it stable. It took between 1-2 hours of careful manual polishing under the microscope with many control steps in between. At the end we pasted immediately the slab on the actual sample holder and placed it inside the vacuum chamber.

Chapter 5

Non-equilibrium spectroscopy

The time- and frequency-resolved optical spectroscopy out of equilibrium allows us to study the changes of the optical properties, such as the reflectivity, over a wide spectral window. This is the key feature that enable us to identify the microscopic mechanisms responsible for the optical variations through an appropriate modeling. On the other hand, the temporal resolution permits to follow the relaxation dynamics of the electronic population after an impulsive optical excitation. As explained in detail in the previous chapter, reflectivity measurements are performed through the pump & probe techinique, that allows us to obtain both subpicosecond temporal resolution, thanks to the short temporal duration of both pump and probe pulses and the suitable delay between them, and frequency resolution in the visible- near IR spectral region, by means of supercontinuum light generation in a non-linear optical fiber. In Fig. 5.1 we highlight by a dashed box the portion of the reflectivity curve $R_{eq}(\omega)$ that we explore by means of our supercontinuum probe. Measurements on two Hg1201 samples at different doping are performed: on an optimally-doped (OD) sample with $T_c = 96$ K and ad underdoped (UD) sample with $T_c = 55$ K.

In this chapter we will discuss the time- and frequency-resolved reflectivity variation measurements, $\Delta R/R(\omega, \tau)$, performed in normal state, in the pseudogap state and in

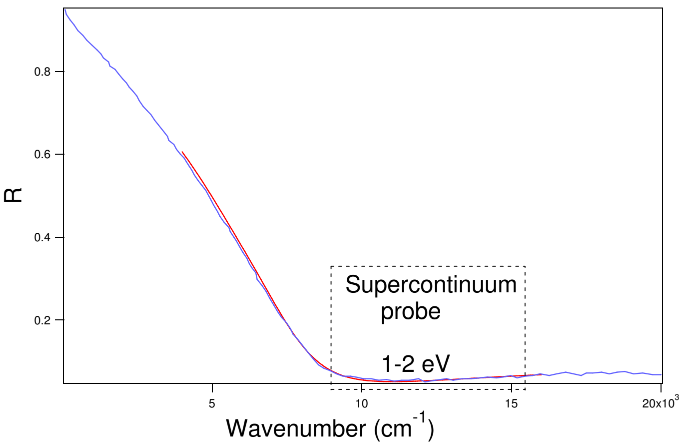

Figure 5.1: Equilibrium reflectivity of Hg1201 at 300 K. The spectral range of our supercontinuum probe is marked by the dashed edge.

the supercontucting phase by the monochromatic pump-supercontinuum probe set-uo described in section 4.4. In order to study the relaxation dynamics of the electronic distribution after the pump-induced excitation, time-resolved reflectivity variation data $\Delta R/R(\tau)$ at a fixed probe photon energy (1.55 eV) are discussed. Since a photoexcitation induces an impulsive variation in the optical properties due to changes in the dielectric function, by the reflectivity variation soon after a pump-induced excitation over a wide spectral range we are able to determine the microscopic origin of these changes. Therefore we report the spectral traces $\Delta R/R(\omega, \tau = 0)$ at zero time delay. Both traces, at fixed photon energy and at fixed delay, and are extracted by the time-energy matrix of the variation reflectivity, i.e. the $\Delta R/R(\omega, \tau)$. Finally, we complete our study on both the OD and UD Hg1201 samples in the pseudogap state by showing the temperature-dependent measurements performed by the one color (1.55 eV) pump-probe experimental set-up.

5.1 The differential model

In order to interpret the spectral response reported in this chapter, we use a differential model for the optical reflectivity based on the Extended Drude Model (EDM). From the previous chapter, a $\Delta R/R(\omega,\tau)$ signal is defined as

$$\frac{\Delta R}{R}(\omega,\tau) = \frac{R_{ex}(\omega,\tau) - R_{eq}(\omega)}{R_{eq}(\omega)} \tag{5.1}$$

where $R_{ex}(\omega,\tau)$ is the time-dependent pump-excited relfectivity and the $R_{eq}(\omega)$ is the reflectivity at equilibrium. According to the formula 2.11, the reflectivity is determined by the dielectric function, thus a variation in the reflectivity is intrinsically related to a variation in the dielectric function, i.e. in the electronic properties.

As explained in chapter 3.2, R_{eq} is well described by the EDM. The parameters used to interpolate R_{eq} has been also reported. In order to reproduce the $\Delta R/R(\omega)$ at a fixed time delay, some parameters are changed and the difference from the equilibrium reflectivity function is calculated. The best fit is the one that minimize the difference bewteen the calculated $\delta R/R$ and the $\Delta R/R$ data by varying the minimum number of parameters, in order to have a better control on each contribution.

5.2 The optimally-doped Hg1201 sample

Fig. 5.2 reports the $\Delta R/R\,(\omega,\tau)$, as measured by the supercontinuum probe on the OD Hg1201 sample at different temperatures: at T = 11 K, the sysyem lies in the superconducting phase, at T = 120 K and T = 150 K, in the pseudogap state, at T = 300 K, in the normal state.

Measurements in the superconducting phase and in the pseudogap state are performed at pump fluence well within linear regime of the optical response, an estimate of that range in the superconducting phase is reported in section 5.3.4. In the normal state the threshold of the linear response is higher and the reflectivity signal weaker than that in

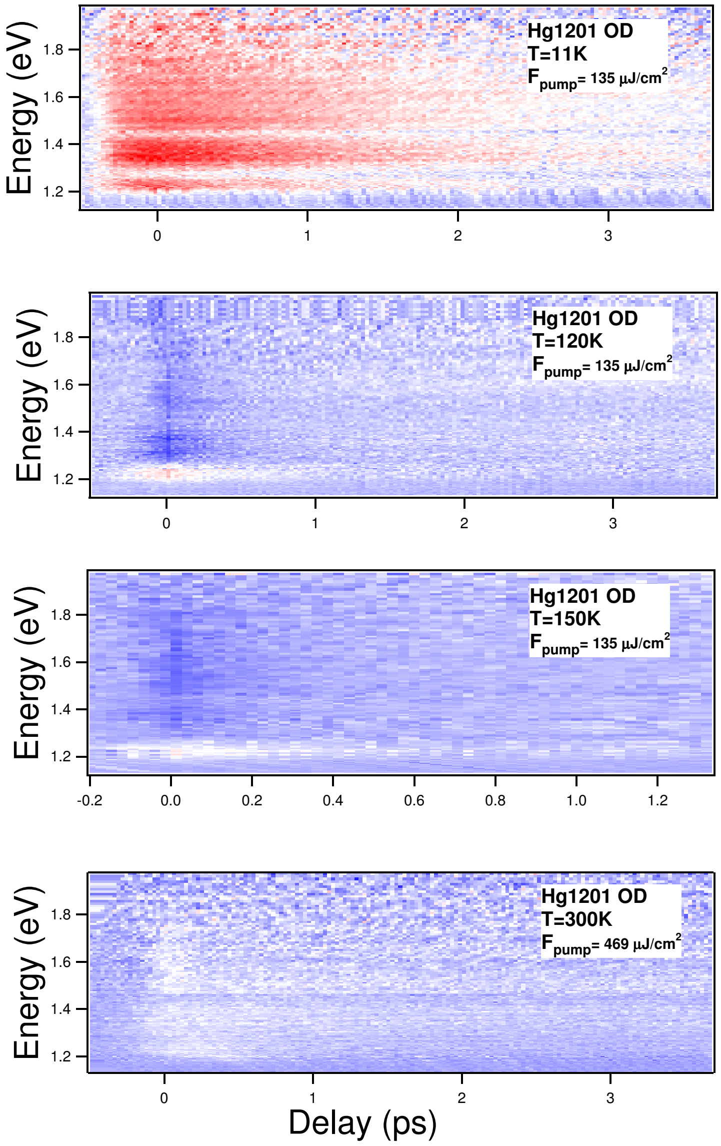

Figure 5.2: The $\Delta R/R(\omega,\tau)$ measured on an OD Hg1201 sample in the 1-2 eV spectral region at different temperatures: 11 K (superconducting phase), 120 K and 150 K (pseudogap state), 300 K (normal state). In the legend the pump fluence is reported.

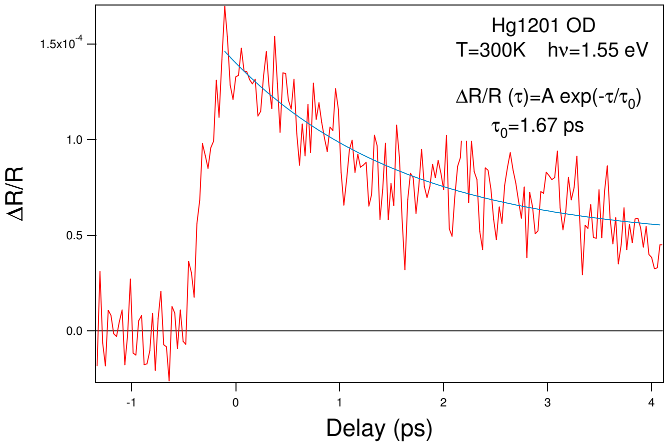

Figure 5.3: The $\Delta R/R\,(\tau)$ data (red line) and the interpolation (blue line) at probe photon energy $\hbar\nu = 1.55$ eV related to the OD Hg1201 sample at 300 K. In the legend the fit function and the two decay times are reported.

the superconducting phase, then we choose a higher pump fluence in order to increase the reflectivity signal.

5.2.1 Normal state

Accordingly to the phase diagram reported in fig. 3.6, at 300 K the OD Hg1201 sample is in the normal state. The corresponding time-resolved optical spectrum in Fig. 5.2 shows a positive reflectivity variation $\Delta R/R\,(\omega,\tau)$ in the whole observed spectral range and at any delay between the pump and the probe pulses.

In fig. 5.3, the $\Delta R/R\,(\tau)$ data at fixed probe wavelenght ($\lambda \sim 800$ nm, $\hbar\omega = 1.55$ eV) are shown, revealing a decreasing signal of the order of 10^{-4}. We fit the data with a decreasing exponential function, whose decay time is reported in the legend. This values account for the relaxation dynamics of the electronic population through a multiple process. In a conventional metal, a useful model used to explain the system thermalization after an impulsive exitacion is the so-called Two- Temperature Model costing in two relaxation processes: a fast thermalization between the electrons decoupled from the lattice within a few hundred femtoseconds, then a slow thermalization of the electrons with the underlying lattice by means of electron-phonon scattering within a few picoseconds. Although our sample is in the normal state at room temperature, this model turns out to be inadeguate on the time scale of hundreds of femtosecond, since in this system the electronic excitation is actually not really decoupled from phonon distribution within this short time scale. Therefore the Three- Temperature Model has to taken into account for the relaxation dynamics of HTSCs in the normal state [13].

Following the Three- Temperature Model, one have to consider bosonic distribution as made up of two subsystems. One of them is composed by high-energy phonons which are strongly coupled to the electronic population, while the other is composed by low-energy phonons which weakly interact with the electrons. Within the first hundreds of femtoseconds excited electrons scatter with the coupled phonons: these are only a small portion of the all phonon spectrum and have a low specific heat, thus they are able to reach the electronic temperature as soon as the pump pulse excites the system, and then they thermalize together with electrons.Than a slow relaxation dynamics occurs by means of electron coupling with the low-energy phonons untill they reach the thermal equilibirum.

In order to identify the contribution in the EDM responsible for the positive reflectivity variation, the maximum $\Delta R/R\,(\omega, \tau = 0)$ is shown in Fig. 5.4. The $\Delta R/R\,(\omega, \tau = 0)$ exhibits a positive reflectivity variation that is higher in the near IR region while it decreases at higher photon energy. The best differential fit to $\delta R/R(\omega, \tau = 0)$ is obtained by slightly increasing the electronic scattering in the EDM. Let us explain what the change of this parameter means. In the simplest picture, as soon as the electrons are excited to an out-of-equilibirum state by the pump pulse, they rapidly relax together with strongly coupled phonons toward the Fermi energy on a subpicosecond timescale.

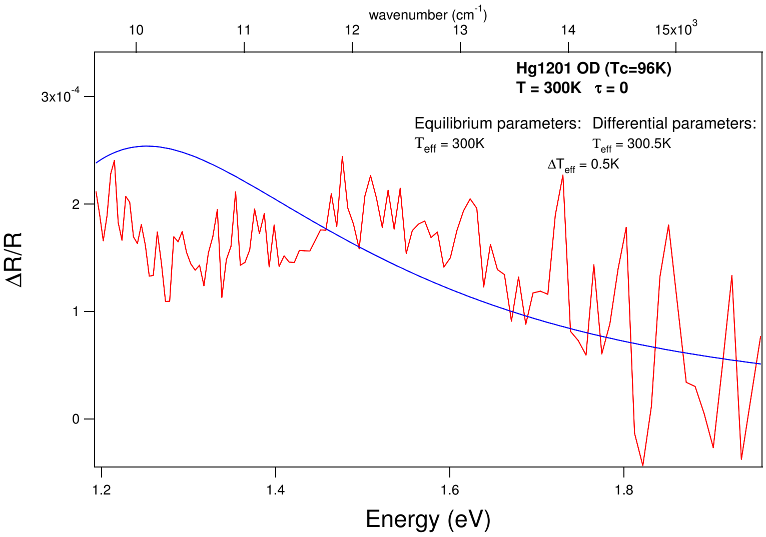

Figure 5.4: The $\Delta R/R\,(\omega,\tau=0)$ data (red line) and the differential fit (blue line) related to the OD Hg1201 sample at 300K.

Since the lifetime of these excitations is so short, an increase in the electron scattering rate occurs. Accordingly to the Drude model for metals, the electron scattering is the origin of a viscous damping of the electron motion which is in turn proportional to the absorption of electromagnetic radiation. Since the radiation lies in the visible-near infrared region, electronic low-energy intraband transition are mainly induced in a metal. Thus we expect that light absorption in the visible-near IR region increses the scattering rate of low-energy electrons. This is shown in reflectivity data by a broadening of the Drude peak around the plasma frequency.

5.2.2 Superconducting phase

In the superconducting phase, a different $\Delta R/R\,(\omega,\tau)$ signal appears in the dynamical spectrum, with a more intense positive variation of the reflectivity and a slower decay time. The time-resolved reflectivity variation at the probe photon energy of 1.55 eV is extracted from the optical spectrum at 11 K and it is shown in Fig. 5.5. The data is

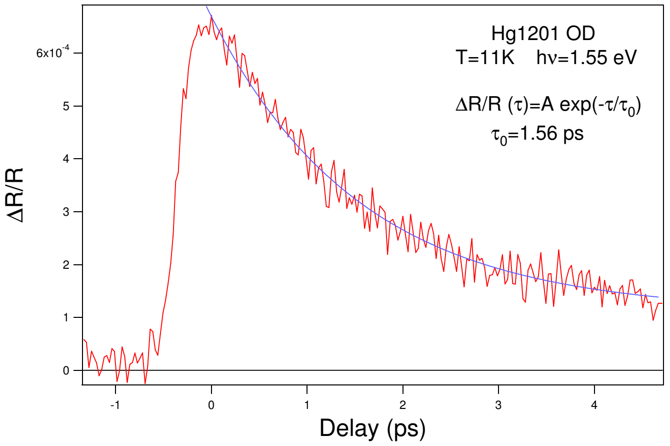

Figure 5.5: The $\Delta R/R\,(\tau)$ data (red line) and the interpolation (blue line) at probe photon energy $\hbar\nu = 1.55$ eV related to the OD Hg1201 sample at 11 K. In the legend the fit function and the decay time is reported.

well fitted by a single exponential decay with a long relaxation time of 1.56 ps.

A useful model to interpret the relaxation dynamics of photoexcited superconductors is the Rothwarf-Taylor model, which is based on the following equations:

$$\dot{n} = I_{QP}(t) + 2\eta N - \beta n^2 \tag{5.2}$$

$$\dot{N} = I_{ph}(t) + 2\eta N - \beta n^2/2 - \gamma_{esc}\,(N - N_T) \tag{5.3}$$

describing the density of excitations n copuled to phonons, N being the gap-energy phonon density. The non-equilibrium quasi-particles (i.e. fermions) and phonons are photo-injected in the system through the source terms $I_{QP}(t)$ and the $I_{QP}(t)$. In this model, two electrons recombine to form a Cooper pair emitting a boson with energy larger than 2Δ, where Δ is the superconducting gap. Since the reverse process is also allowed, the relaxation dynamics is determined by inelastic phononic processes. The electronic and phonon population are indeed photo-injected by the pump laser and an

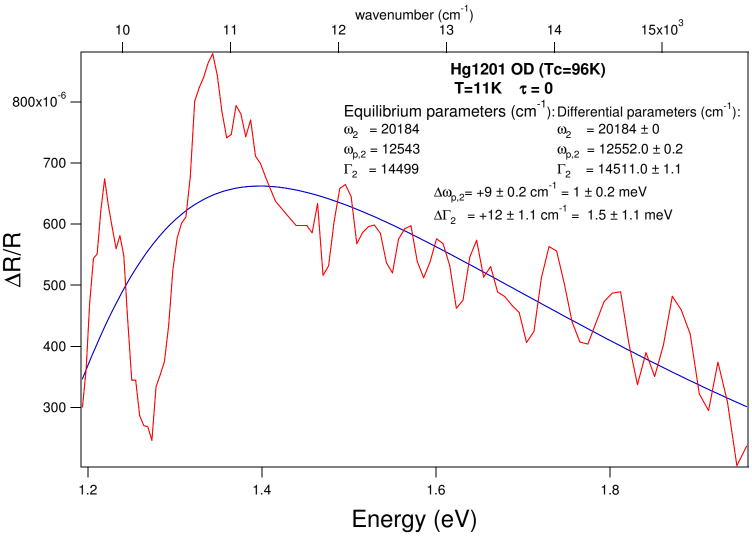

Figure 5.6: The $\Delta R/R\,(\omega,\tau=0)$ data (red line) and the differential fit (blue line) related to the OD Hg1201 sample at 11 K.

out-of-equilibrium state is impulsively eshablished in the system. Then the coupling between electrons and phonons is obtained through the annihilation of a Cooper pair via gap phonon absorption and the emission of gap phonons during the two-boby recombination of excitations to form a new Cooper pair. As long asl the emitted phonons mantain an energy larger than 2Δ, the reformation of Copper pairs is bottlenecked and the relaxation of $\Delta R/R\,(\tau)$ is slowed with respect to the dynamics in the normal state. Thus the excitation relaxation in the superconducting phase is ultimately regulated by the escape rate of the non-equilibirum gap-energy phonons.

Fig. 5.6 shows the variation of the optical response in the 1-2 eV spectral region at zero delay and the corresponding best differential fit through the EDM. The $\Delta R/R\,(\omega,\tau=0)$ can not be reproduced by variation in the only Drude component of the EDM, since not only intraband transitions are involved. Actually the $\delta R/R\,(\omega,\tau=0)$ is reproduced by increasing the values of the spectral weight $\omega_{p,2}$ and the linewidth factor Γ_2 of a high-frequency Lorentz oscillator at 2.5 eV, which accounts of a high-energy interband

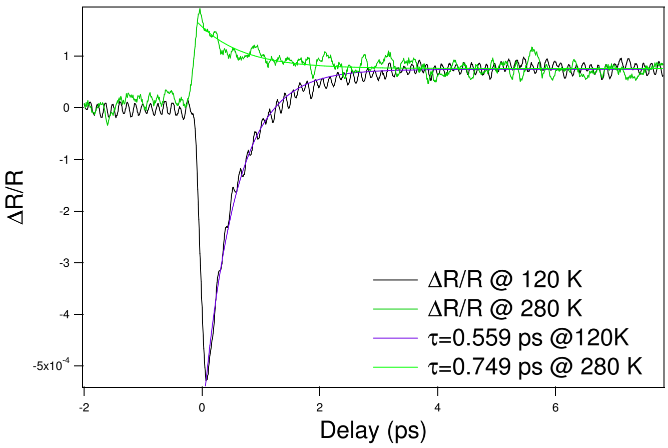

Figure 5.7: $\Delta R/R(\tau)$ at fixed phonon energy (1.55 eV) with the the system in the pseudogap state (T = 120 K, black line) and in the normal state (T = 300 K, green line). The decay times from the interpolation are shown in the legend: $\tau_{120K} = 0.599 \pm 0.004$ ps, $\tau_{280K} = 0.749 \pm 0.038$ ps.

transition. The result is in agreement with measurements performed on similar compounds at equilibrium and out-of-equilibrium and reported in the literature [8, 18].

5.2.3 Pseudogap state

One of the key feature of the high temperature superconductors is the onset of a pseudogap in the density of state (DOS) at temperatures between the critical temperature of the superconducting phase transition and a temperature T^* that depends on the sample doping. Therefore, although in the normal state an almost constant DOS at the Fermi level can be considered, this approximation fails as the temperature decreases and a pseudogap opens in the electornic DOS. The reflectivity variation measured below the pseudogap temperature T^* as soon as the pump excites the system is also completely different from that measured in normal state. Thus an evolution of the EDM, accounting for a non-constant electronic DOS, becomes necessary [27].

Actually, to mimic the opening of a gap, the gap filling parameter N is added to the model. As this parameter is equal to 1, the gap is completelly filled or likewise the system is in the normal state. A decrease in the N paratemeter means that empty levels appear in the electronic DOS. Thanks to this improvement, in the EDM it is possible to calculate the best fit to the $\Delta R/R(\omega)$ data even in the presence of a pseudogap.

Measurements on an OD Hg1201 sample in the pseudogap state are performed at two different temperatures, i.e. at T = 120 K and T = 150 K. In both cases the $\Delta R/R\,(\omega,\tau)$ signal observed within few hundreds of femtoseconds after the pump excitation is positive below 1.3 eV, while it is negative above this energy. After a few picoseconds the optical response in the whole spectral region exhibits the same characteristics of the normal state. This feature is more evident if we look at the relaxation dynamics of the reflectivity variation at a fixed photon energy in the pseudogap and in the normal state. Therefore in Fig. 5.7 we report the $\Delta R/R(\tau)$ data at T = 120 K with the system in the pseudogap state and at T = 280 K with the system in the normal state performed by monochromatic (1.55 eV) pump-probe technique. We see that the reflectivity variation looks different within the first 2 ps, since it is positive in the normal state and negative in the pseudogap state, while for further decays the $\Delta R/R(\tau)$ at T = 120 K joins that at T = 280 K and they overlap perfectly, both showing a positive decreasing signal typical of the $\Delta R/R(\tau)$ of Hg1201 compounds in the normal state. Acutually both decay times are of the order of few hundreds picosecond, thus faster than the relaxayion dynamics in the superconducting phase, showing that in preudogap state any bottleneck in the reformation of Cooper pairs occurs.

The spectral trace at zero time delay extracted from the $\Delta R/R\,(\omega,\tau)$ spectra of the UD Hg1201 sample at 150 K is presented in Fig. 5.8. The best fit to the data is also shown together with the differential parameters we used to reproduce the reflectivity variation induced by the pump pulse. The differential fit indicates a transient increase in the fill-

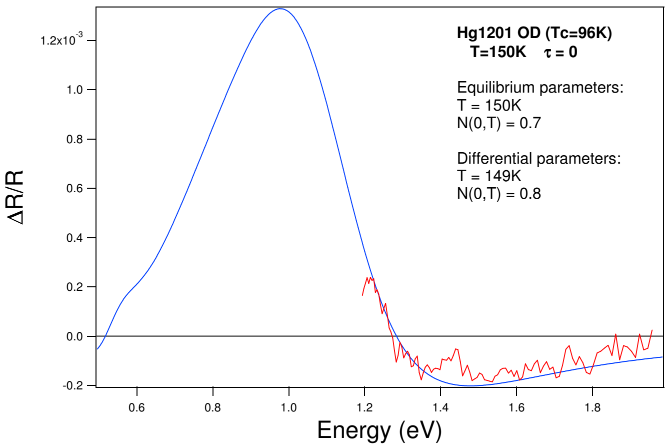

Figure 5.8: The $\Delta R/R\,(\omega, \tau = 0)$ data (red line) and the differential fit (blue line) related to the OD Hg1201 sample at 150 K.

ing of the gap and a decrease of the electronic scattering rate. Thus two pump-induced processes can be analyzed: the impulsive filling of the pseusogap, as a consequence of the photoinjection of excitations, rapresented by a quench in the N parameter from 0.7 to 0.8 and the impulsive decrease of the scattering rate that we explain as effect of the strong electronic correlations that characterize all cuprates. This surprising effect has been already observed on a similar compound, the Y-Bi2212 [28]. We remark that this behaviour vanishes at longer delays.

In order to explain the decrease of the electronic scattering rate within few hundreds of femtoseconds after the pump-induced excitation, we remind the approximated expression of the memory function

$$M\left(\omega\right) = -2\int_{0}^{\infty} \alpha^{2}F\left(\omega'\right) L\left(\omega, \omega', T\right) d\omega'. \tag{5.4}$$

We point out that actually the memory function is a complex quantity, where the imaginary part is related to the electron-phonon scattering and expresses the electronic scattering rate.

By the formula (5.4) we note that the temperature dependance lies in the kernel function $L(\omega, T)$ since it accounts for the electronic and bosonic distribution, while the strenght of the electron-phonon coupling is temperature-independent. A photoexcitation acts by heating the system, thus changing the contribution in the integral (5.4) due to the kernel function. An increase in the scattering rate is expected.

As we deal with strong correlated system, such as Hg1201 compounds, a more complex glue function has to be considered, as explain in section 2.3.2. Suppose that the glue function is also temperature-dependent and decreases as soon as the population is driven out of equilibrium. In this case, the conventional increase in the scattering rate can be compensate by an impulsively decrease of the glue, even decreasing within few hundreds picoseconds.

Since this effect exhibits only in an out-of equilibrium scenario and any equilibirum spectroscopy, such as ARPES or STM, is able to reveal it, the origin must lie in a faster and more energetic interaction than the electron-phonon coupling. Equilibrium measurements investigate indeed nodal excitations that occur on an energy scale of 40 meV in which electronic and phononic excitations coexist. Out-of-equilibrium measurements allow us to disenangle electronic and bosonic distribution and access to the anti-nodal excitations.

As explained in section 3.1.3, ARPES data reveal a gapless density of states along the nodal direction of the first Brillouin zone of cuprates, which corresponds to the diagonal of the square direct lattice. On the contraty, a gap opens along the anti-nodal direction, which corresponds to the side of the square. Dynamical mean field theory (DMFT) calculations are obtained considering only a single unit cell and ignoring any coupling except for electronic correlations. A metallic behavior around the nodal point is calculated, where electrons experience weaker Coulomb repulsion, thus by heating in that region an increase in the scattering rate is expected. At the anti-nodes the correlations are stronger and consequently the charges are more localized, thus a gap opens in the electronic DOS. In this case, by heating the system electrons are excited and tends to delocalize exhibiting an almost metallic behavior with a minor scattering rate than that in the localized state. We stress the fact that electron-phonon coupling is suppressed in the calculations.

Experimentally we reproduce a system characterized by only electron correlations by means of an ultrafast excitation that decouples electronic and bosonic population within a subpicosecond time scale. In this scenario a temporary decrease of the scattering rate is allowed and explained in terms of a decrease in the glue function and an impulsive delocalization of the excited electrons.

5.2.4 One color temperature-dependent data

In the previous section we have investigated the variation of the optical properties of doped Hg1201 compounds due to changes in the electronic structure by a pump-induced excitations. In this chapter the temperature-dependent reflectivity variation $\Delta R/R\,(\tau)$ are reported in order to explain the behaviour of the system in the pseudogap state as the temperature increases. Fig. 5.9 shows the time-resolved reflectivity variation at different temperatures with a monochromatic probe ($\lambda = 800$ nm). The data are performed on an OD Hg1201 sample from 120 K up to 300 K.

At lower temperatures the system lies in the pseudogap state and the reflectivity variation is negative at any delay accordingly to the $\Delta R/R\,(\tau)$ extracted from the time-energy matrix $\Delta R/R$ at the same temperature. At about 170 K a change in the sign of the signal appears within the first 100 fs, while for further delays the reflectivity variation restores the negative sign. By heating further the sample, the positive peak increase more and more untill the negative contribution to the data is suppressed. At about 240 K a positive reflectivity variation is observed at any delay, which resembles the time-resolved spectra $\Delta R/R\,(\tau)$ obtained in the normal state at room temperature.

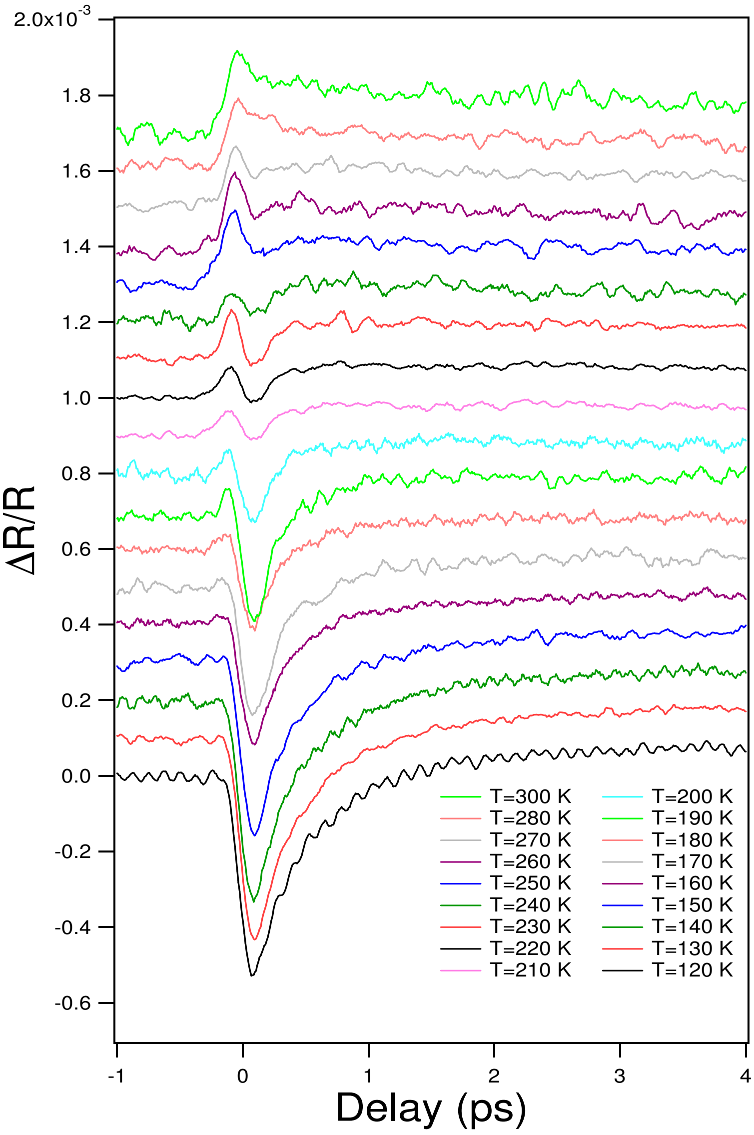

Figure 5.9: The temperature dependent $\Delta R/R(\tau)$ performed on an OD Hg1201 sample from 120 K up to 300 K. At 170 K a change in the sign of the $\Delta R/R(\tau)$ appears, revealing the transition of the system from the pseudogap state to the normal state.

Then, by heating the sample above 240 K, the system is driven out from the pheudogap phase as would be expected by the phase diagram shown in 3.6 and the normal state is established in the system.

5.3 The underdoped Hg1201 sample

In order to confirm the results explained in the previous section, we report the dynamical spectra of the reflectivity variation performed in the superconducting phase and in the pseudogap state, as measured on a UD Hg1201 sample ($T_c = 55$ K) by a supercontinuum probe. We also show the one color (1.55 eV) data performed at different temperatures in the pseudogap state. At the end of this chapter we repot the one color (1.55 eV) data performed in the superconducting phase at difference pump fluences in order to obtain the range of linear response of the system.

5.3.1 Superconducting phase

The $\Delta R/R$ data performed at T = 20 k on the UD Hg1201 are reported in Fig. 5.10. We see that the reflectivity variation is positive at lower energy, while negative above $\sim$ 1.55 eV. It is not possible to explain why this happens by comparing the sign in the reflectivity variation only at one probe wavelenght, since many different contributions in the EDM could account for the same reflectivity variation at a single frequency. A wide spectral range resolution is what allows us to identify the actual contribution. Therefore in fig. 5.11 we show the $\Delta R/R\,(\omega, \tau = 0)$ data and the differential fit calculated by EDM.

The best differential fit to the data is calculated by varying the parameters of a high frequency Lorentz oscillator. In particular, this is the same Lorentz oscillator used to obtain the best differential fit in the case at optimal doping. Thus the same high-energy interband transition changes after the electrons are excited by the pump pulse, inspite of at first sight the $\Delta R/R\,(\omega, \tau = 0)$ data at 20 K looks very different from that measured

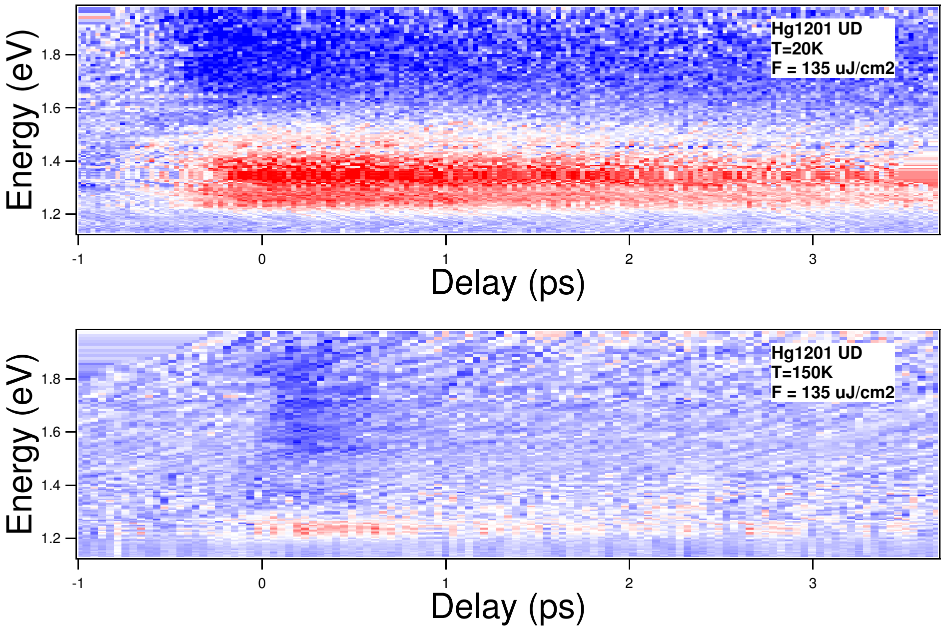

Figure 5.10: The $\Delta R/R(\omega,\tau)$ measured on an UD Hg1201 sample in the 1-2 eV spectral region at different temperatures: 20 K (superconducting phase) and 150 K (pseudogap state). In the legend the pump fluence is reported.

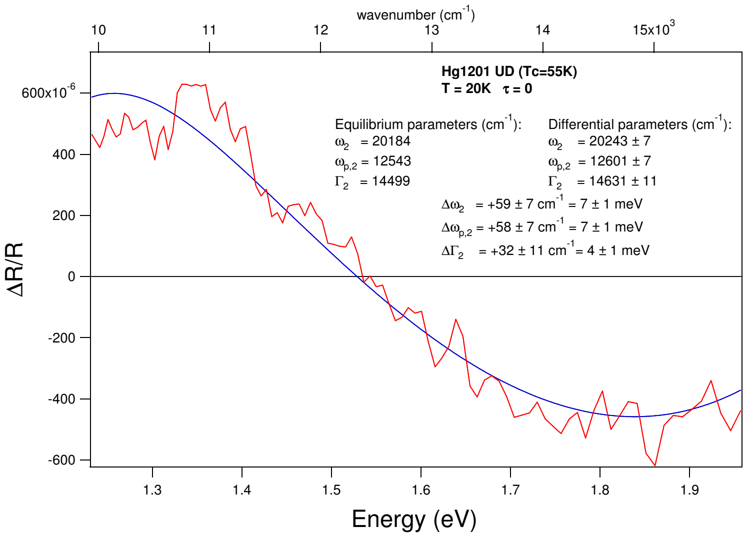

Figure 5.11: The $\Delta R/R\,(\omega, \tau = 0)$ (red line) and the differential fit (blue line) of an UD Hg1201 sample at 20 K.

on the Hg1201 sample at optimal doping. Notice that this contribution due to a high energy Lorentz oscillator describes a typical behavior of the superconducting phase, since neither in the normal state nor in the pseudogap state we need to change any parameters of the Lorentz oscillators in order to reproduce the $\Delta R/R\,(\omega, \tau = 0)$ data.

5.3.2 The pseudogap state

In Fig. 5.12 the $\Delta R/R\,(\omega, \tau = 0)$ performed on the UD Hg1201 sample at at 150 K is shown together with the best differential fit. The meaningful parameter in order to obtain the best fit are the filling parameter N, that accounts for the photoinduced pseudogap closing, and the scattering rate. As observed on the OD sample in the pseudogap state, an impulsive suppression of pairing occur since N increases from 0.7 to 0.8 while the scattering time decrease slightly. For an interpretation of the data and the fitting parameters we refer to the OD case.

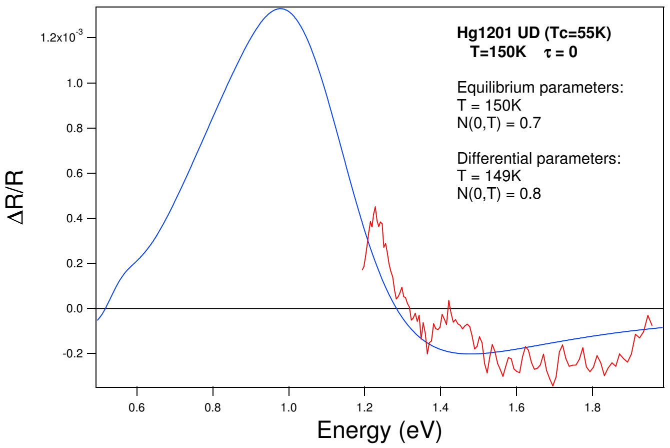

Figure 5.12: The $\Delta R/R\,(\omega, \tau = 0)$ (red line) and the differential fit (blue line) of the UD Hg1201 sample at at 150 K.

5.3.3 One color temperature dependent-data

In Fig. 5.13 time-resolved reflectivity variation at different temperatures is shown. The data has been taken on the UD Hg1201 sample from 250 K up to 325 K with a monochromatic probe. With respect to the previous temperature-dependent measurements on the OD sample, we are not able to reach the critical temperature in order to drive out the system from this phase. These data indeed does not show any change in the reflectivity signal, but rather the expected negative dynamics according to the data in the pseudogap state. This result is in agreement with the predictions by the phase diagram, since in UD systems the pseudogap state occurs over a wide energy scale above the critical temperature T_c. The end of the pseudogap state is expected at a temperature higher than 350 K.

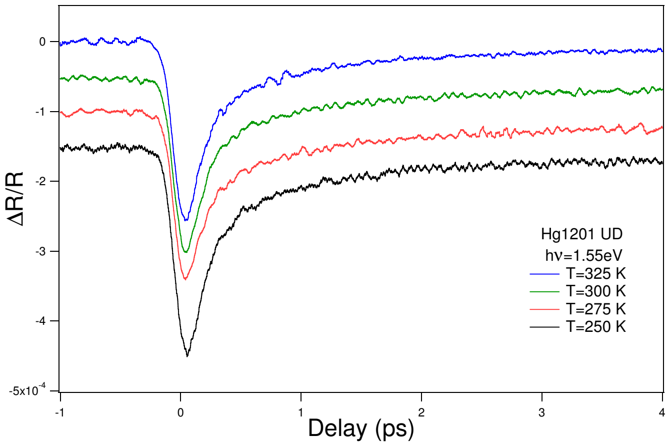

Figure 5.13: The temperature-dependent $\Delta R/R\,(\tau)$ performed on the UD Hg1201 sample from 250 K up to 350 K. Any change in the sign of the reflectivity variation appears: by heating the sample up to 350 K the system still remains in the pseudogap state.

5.3.4 One color fluence dependent measurements

We report measurements performed on the UD Hg1201 sample in the superconducting state in order to esimate the linear regime of the optical response. We observe a linear response by varying the pump fluence up to 176 $\mu J/cm^2$. Thus we confirm that the $\Delta R/R$ data are performed on OU and UD sample well within the linear regime. METTERE FIGURA!!!!!

Chapter 6

Conclusion

In this work we have provided a rich overview of the out-of-equilibrium optical response of mercury-based high-temperature superconductors (Hg1201). Thanks to careful and thorny sample preparation, measurements on these compounds have been successfully performed by broadband optical spectroscopy in our lab for the first time. Mercury-based compounds can be considered a prototypical system for a larger class of high-T_c supercoonductors, i.e. the cuprates, because of its high ordered crystal structure and the presence of a single Cu-O layer between the charge reservoir. Two Hg1201 samples have been studied: an optimally doped with critical temperature $T_c = 96$ K and an underdoped sample with $T_c = 55$ K. The normal state, the pseudogap state and the superconducting phase have been investigated in this systems.

The frequency resolved transient reflectivity variation have allowed us to access the changes in the electronic properties soon after high-energy excitation induced by a pump laser pulse. The data has been reproduced through the Extended Drude Model and they confirm previous results on a different compound, the Y-Bi2212, thus providing a more general description of the behavior of this systems. Probing the system in the normal states, we have observed an almost metallic behavior with an increasing electronic scattering rate as the population is driven out of equilibrium by a pump pulse. A completely different behavior appear investigating the superconducting phase of the system, since an increasing spectral weight of high energy interband transitions accounts for the reflectivity variation. Probing in the pseudogap state, we have taken advantage of the possibility to excite the system strongly out-of-equilibrium by means of IR radiation and to investigate the electronic electronic distribution in the first few hundreds of femtoseconds after the photoexcitation, in order to disentangled the electronic from the phononic contribution. This is a peculiarity of this spectroscopy technique, providing a powerful tool to unravel the microscopic mechanisms involved in the pseudogap state. The EDM has been modified in order to reproduce the data in the pseudogap state. Since a non-constant electronic density of states characterizes the class of cuprates in the pseudogap state, a filling gap parameter has to be use in order to account for the photoinduced suppression of the gap in the first few hundreds of femtoseconds.

Thanks to the time resolution on the subpicosecond scale, we have been able to controll the relaxation dynamics of electrons. The reflectivity variation in the normal and in the pseudogap state decays fast, while much slower in the superconducting phase, showing a bottelnecked in the recombination of Cooper pairs.

Temperature-dependent measurements habe been performed on both OD and UD compounds in the pseudogap state, confirming the doping dependance on the gap energy scale.

A possible prosecution could deal with other Hg-based cuprates at different doping in order to obtain a more detailed phase diagram of this prototypical high-T_c superconductor.

Since by exciting the system with infrared light we are inducing a strongly non-thermal charge distribution, while the superconducting pairing occurs in cuprates on energy scales is of the order of tens of meV, it could be very interesting to investigate these systems through optical pump-ThZ probe spectroscopy. In fact, thanks to the low-energy of the probe pulse, comparable to the superconducting gap, we would be able to investigate the dynamics of the population partecipating in the condensate after a strong excitation is photoinduced in the system, eventually leading to unravel the glue mechanism at the origin of pairing in HTSCs.

Moreover the combination of improved models for the interaction of ultrashort light pulses with unconventional supercnductors and more advanced experimental techniques will be certainly a key strenght in understanding the mechanism that leads to high-temperature superconductivity.

Appendix A

The Kerr Lens Mode-Locking

The technique used to mode-lock the Mira laser, i.e. to produce ultrashort laser pulses on the order of 10^{-12} - 10^{-15} seconds, is called *Kerr Lens Mode-Locking* (KLM). The mode-locking mechanism consists in inducing a phase relation between each mode inside the laser resonance cavity. If modes with random time-dependent phase interfere, the output will be an almost constant signal (*continuous wave laser operation*), while if they interfere constructively, we'll obtain trains of powerful pulses (*phase locked laser operation*). The temporal separation τ between two successive pulses corrisponds to the time taken for the light to make exactly one round trip of the laser cavity and it is determined by the geometry of the cavity and by the distance L between the mirrows, according to the formula $\tau = 2L/c$, where c is the speed of light. The inverse of this time gives the number of pulses per second, commonly reffered to as the repetition rate. In the Mira laser τ is approximately 13.2 ns, which corresponds precisely to a repetition rate of 76 MHz .

The method of *Kerr Lens Mode-Locking* exploits a non linear optical process, known as Kerr effect, according to which the index of refraction n of the non linear optical medium depends on the intensity of the applied electric field, therefore on its quadratic power. In fact, at sufficiently high intensity, the electric field associated with the light

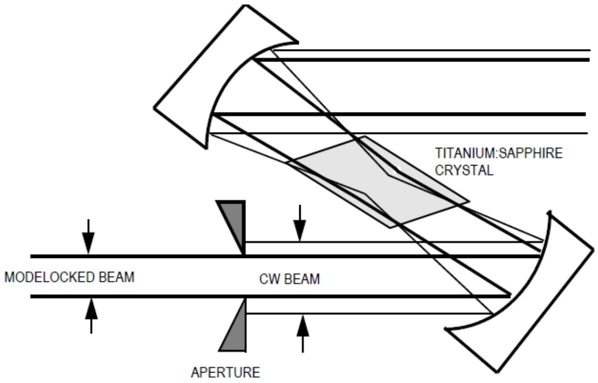

Figure A.1: Scheme of Kerr Lens Mode-Lockin.

can distort the atoms of the gain medium and alter its index. The profile and the power density spatial distribution of a laser beam is tipically gaussian. Therefore, while the beam propagates through the medium, it ”experiences” a different index of refraction along its profile: n is greater at the peak intensity of gaussian beam. It results in a self-focusing process which is much stronger in a mode-locked laser beam than in a continuous wave (CW), as shown in Fig. A.1, and this is due to an increased overlap between the pumped gain profile and the circulating cavity mode. The active medium is the Titanium:Sapphire crystal in the Mira laser. To favour pulsed mode, the cavity is made unstable against CW operation by an aperture positioned where the beam focuses most, so minimizing round trip losses.

In addition to the self-focusing effect, pulses in ultrafast laser is also affectec by self-phase modulation (SPM). When an ultrashort pulse enters the medium, it induces a local index of refraction that is dependent on the light field intensity as a result of Kerr effect. This variation causes a phase shift $\varphi(t)$ in the time domain inside the pulse

$$\varphi(t) = \omega_0 t + \frac{\omega_0(n_0 + n_2 I(t))}{c} z \tag{A.1}$$

therefore a change in the pulse spectrum

$$\omega(t) = \frac{\partial \varphi}{\partial t} = \omega_0 + \frac{\omega_0 n_2 z}{c}\frac{\partial I(t)}{\partial t}. \tag{A.2}$$

Since the group velocity dispersion (GVD) of the wave packet is negative inside the medium, the temporal resharping of wave packets induced by SPM can be offset, preserving the temporal profile of travelling pulses.

Appendix B

The lock-in amplifier

Let us show in more details, how the signals are processed inside the Lock-in amplifier (see fig. B.1). We choose a simply example in which the input signal is described by

$$V_S(t) = V_{0_S} \sin(\omega_r t + \theta_s), \tag{B.1}$$

and the reference signal is

$$V_L(t) = V_{0_L} \sin(\omega_L t + \theta_{ref}). \tag{B.2}$$

They pass through a phase-sensitive detector (PSD) that multiplies together the signals and returns an output signal in the form of:

$$V_{PSD}(t) = V_{0_S} V_{0_L} \sin(\omega_r t + \theta_s) \sin(\omega_L t + \theta_{ref}). \tag{B.3}$$

Taking advantage of Werner formula, we can rewrite (B.3) in the form of a sum of two AC signals:

$$\begin{aligned} V_{PSD}(t) = & \frac{1}{2} V_{0_S} V_{0_L} \cos\left[(\omega_r - \omega_L)t + (\theta_s - \theta_{ref})\right] + \\ & - \frac{1}{2} V_{0_S} V_{0_L} \cos\left[(\omega_r + \omega_L)t + (\theta_s + \theta_{ref})\right]. \end{aligned} \tag{B.4}$$

A low pass filter is used to select the only component with $\omega_r = \omega_L$, i.e. the DC signal:

$$V_{PSD} \frac{1}{2} = V_{0_S} V_{0_L} \cos(\theta_s - \theta_{ref}), \tag{B.5}$$

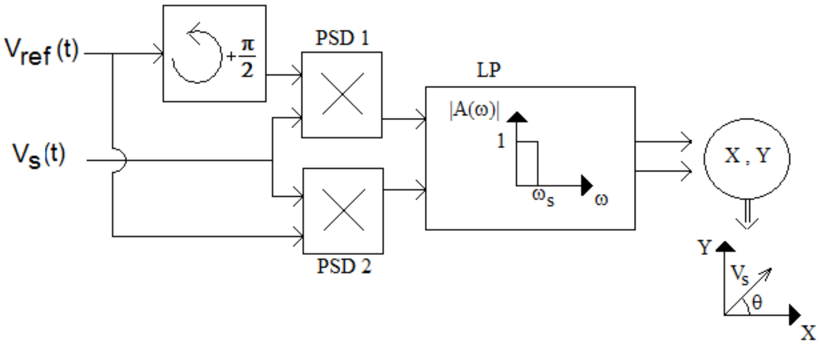

Figure B.1: Scheme of the lock-in components.

and a phase-locked loop (PLL) links together the two phases, so

$$V_{PSD}\frac{1}{2} = V_{0_S}V_{0_L}\cos(\theta), \tag{B.6}$$

where $\theta = \theta_S - \theta_{ref}$.

In order to remove the phase dipendance in the output signal, a second PSD multiplies the signal with a reference shifted by 90 degrees, then a second low pass filter select the DC component

$$V_{PSD} = \frac{1}{2}V_{0_S}V_{0_L}\sin(\theta). \tag{B.7}$$

Thus, we define

$$\begin{cases} X = V_S\cos\theta, & \text{in-phase componenti} \\ Y = V_S\sin\theta, & \text{quadrature component} \end{cases} \tag{B.8}$$

so we obtain

$$\begin{cases} \sqrt{X^2+Y^2} = V_S. \\ \theta = \arctan\frac{X}{Y} \end{cases} \tag{B.9}$$

List of acronyms

ARPES	Angle resolved PhotoEmission Spectroscopy
BCS	Bardeen-Cooper-Schrieffer
CW	Continuous Wave
DOS	Density of States
EDM	Extended Drude Model
FWHM	Full Width at Half Maximum
GVD	Group Velocity Mismatch
HTSC	High Temperature SuperConductor
IR	InfraRed
KLM	Kerr Lens Mode-Locking
OD	Overdoped
PSD	Phase Sensitive Detector
SPM	Self-Phase Modulation
STM	Scanning Tunneling Microscopy
UD	Underdoped

Bibliography

[1] Grosso, Pastori, Parravicini, *Solid state physics*, Academic Press (2000)

[2] Tinkham, *Introduction to superconductivity*, Mc-Graw-Hill ,Inc. (1996)

[3] Phillips, *Advanced solid state physics*, Wastview Press (2003)

[4] Kittel, *Introduction to solid state physics*, J. Wiley & Sons,Inc. (1996)

[5] Anderson, *Science*, 235, 1196 (1987)

[6] Anisimov et al.,*Sov. Phys.* JETP 39, 375 (1975)

[7] Basov et al., *Rev. Mod. Phys*, 85(2), 471 (2011)

[8] Basov et al., *Rev. Mod. Phys.*, 83, 2 (2011)

[9] Batlogg et al., *Physica C*, 130, 235–40 (1994)

[10] Chakravarty *Phys. Rev. B* 63, 094503 (2001)

[11] Chang et el., *Nature Phys.*, 8, 871–876 (2012)

[12] Cilento et al., arXiv:submit/0672606 [cond-mat.mtrl-sci] (Mar 2013)

[13] Dal Conte et al., *Science*, 335, 6076 (2012)

[14] Damascelli et al., *Rev. Mod. Phys.*, 75 (April 2003)

[15] Eisaki et al., *Phys. Rev. B*, 69, 064512 (2004)

[16] Emery et el., *Phys. Rev. Lett.*, 58, 2794–2797 (1987)

[17] Emery et el., *Nature*, 374,4347 (1995)

[18] Giennetti et al., *Nat. Commun.*, 2, 353 (2001)

[19] Hüfner *Rep. Prog. Phys.*, 71, 062501 (2008)

[20] Y. Li et al., *Nature*, 455, 372 (2008)

[21] Mirzaei et al., *PNAS*, 110, 15 (2013)

[22] Putilin et el., *Nature*, 362, 226 - 228 (1993)

[23] Varma, *Phys. Rev. Lett.* 83, 3538–3541 (1999)

[24] Kresin, Wolf, *Rev. Mod. Phys.*, 81, 481 (2009)

[25] Testardi, *Phys. Rev. B* Vol.4, No.7, page 2189 (1971)

[26] Zhao Li et al., *Adv. Mat.*, SLAC-PUB-12400 (2007)

[27] Sharapov et al., *Phys. Rev. B*, 72, 134506 (2005)

[28] Cilento, *Dinamiche elettroniche fotoindotte in superconduttori ad alta temperatura critica*, Università Cattolica del Sacro Cuore, Brescia (2008)

[29] http://www.ncnr.nist.gov/equipment/displex.html